Review Article

High *b*-value q-space analyzed diffusion-weighted MRS and MRI in neuronal tissues – a technical review

Yoram Cohen[1]* and Yaniv Assaf[1,2]

[1]School of Chemistry, The Raymond and Beverly Sackler Faculty of Exact Sciences, Tel Aviv University, Ramat Aviv, Tel Aviv, 69978, Israel
[2]Wohl Institute for Advanced Imaging, Tel Aviv Sourasky Medical Center, Tel Aviv, 64239, Israel

ABSTRACT: This review deals with high *b*-value **q**-space diffusion-weighted MRI (DW-MRI) of neuronal tissues. It is well documented that at sufficiently high *b*-values (and high **q**-values) neuronal water signal decay in diffusion experiments is not mono-exponential. This implies the existence of more than one apparent diffusing component or evidence for restriction. The assignment of the different apparent diffusing components to real physical entities is not straightforward. However, the apparent slow diffusing component that was found to be restricted to a compartment of a few microns, if originating mainly from a specific pool and if assigned correctly, may potentially be used to obtain more specific MR images with regard to specific pathologies of the CNS. This review examines the utility of analyzing high *b*-value diffusion MRS and MRI data using the **q**-space approach introduced by Callaghan and by Cory and Garroway. This approach provides displacement probability maps that emphasize, at long diffusion times, the characteristics of the apparent slow diffusing component. Examples from excised spinal cord, where the experimental conditions for which the **q**-space analysis of MR diffusion data was developed can be met or approached will be presented. Then examples from human MS patients, where **q**-space requirement for the short gradient pulse is clearly violated, are presented. In the excised spinal cord studies, this approach was used to study spinal cord maturation and trauma, and was found to be more sensitive than other conventional methods in following spinal cord degeneration in an experimental model of vascular dementia (VaD). High *b*-value **q**-space DWI was also recently used to study healthy and MS diseased human brains. This approach was found to be very sensitive to the disease load in MS, compared with other conventional MRI methods, especially in the normal appearing white matter (NAWM) of MS brains. Finally, the potential diagnostic capacity embedded in high *b*-value **q**-space analyzed diffusion MR images is discussed. The potentials and caveats of this approach are outlined and experimental data are presented that show the effect of violating the short gradient pulse (SGP) approximation on the extracted parameters from the **q**-space analysis. Copyright © 2002 John Wiley & Sons, Ltd.

KEYWORDS: diffusion MRI; high *b*-value DWI; **q**-space diffusion; white matter disorders; multiple sclerosis; MS; spinal cord trauma; neuronal degeneration; neuronal maturation

INTRODUCTION

In the last decade, diffusion has become an important contrast mechanism, particularly in MRI of the CNS.[1] Interestingly, diffusion-weighting as a contrast mechanism did not play an important role in the early days of MRI.[2] However, following the seminal papers of Le Bihan[3,4] and the demonstration regarding the high sensitivity of diffusion-weighted MRI (DWI) for early detection of stroke by Moseley *et al.* in 1990,[5] DWI attracted much more interest.[6–10] After the high sensitivity of DWI to experimental acute stroke was demon-

Abbreviations used: ADC, apparent diffusion coefficient; CNS, central nervous system; CSF, cerebral spinal fluid; DW-MRS, diffusion weighted magnetic resonance spectroscopy; DWI, diffusion-weighted imaging; DTI, diffusion tensor imaging; EAE, experimental allergic encephalomyelitis; EAN, experimental allergic neuritis; EM, electron microscopy; EPI, echo planar imaging; FA, fractional anisotropy; FLAIR, fluid attenuated inversion recovery; FT, Fourier transform; MR, magnetic resonance; MRI, magnetic resonance imaging; MRS, magnetic resonance spectroscopy; MS, multiple sclerosis; MT, magnetization transfer; NAWM, normal appearing white matter; PNS, peripheral nervous system; ROI, region of interest; SD, standard deviation; SNR, signal to noise ratio; SGP, short gradient pulse; SP-SHR, stroke-prone spontaneous hypertensive rat; *TE*, time to echo.

strated in hundreds of studies,[11,12] DWI developed, despite its high sensitivity to motion, into a viable clinical routine practiced in many medical centers.[13] In addition, DWI and diffusion-weighted magnetic resonance spectroscopy (DW-MRS) were used extensively with the aim of unraveling the origin of the reduced apparent diffusion coefficient (ADC) of water in ischemic tissue, compared to normal brain tissue.[14,15] DWI was then used to study, *inter alia*, brain tumors,[16] head trauma,[17,18] experimental allergic encephemyelitis (EAE),[19] spreading depression,[20] multiple sclerosis[21] and other CNS pathologies.[22] Diffusion anisotropy, at least in the CNS, was documented at the relative early stages of DWI,[23,24] but the important development was the introduction of diffusion tensor imaging (DTI) by Basser *et al.*[25] DTI provides a means to separate and quantify the isotropic and anisotropic components of the diffusion tensor and is the basis for MR fiber mapping and MRI tractography.[26,27] Recently, DTI has increasingly been used to study different neurological disorders.[28–30]

Until recently, in DWI and DTI studies of neuronal tissues, the experimental data was nearly always analyzed using the well-known Stejskal–Tanner equation.[31] This equation assumes the existence of a single isotropic and unrestricted diffusing component and is given by:

$$E/E_0 = \exp[-\gamma^2 g^2 \delta^2 (\Delta - \delta/3)D] = \exp(-bD) \quad (1)$$

where E/E_0 is the normalized signal attenuation, γ is the gyromagnetic ratio, g is the pulsed gradient amplitude, δ is the pulsed gradient duration, Δ is the time separation between the leading edges of these gradients and D is the diffusion coefficient. In this equation the term $\Delta - \delta/3$ represents the effective diffusion time (for the simple case of rectangular pulse gradients) while the *b*-value represents the overall diffusion weighting in the experiment.[3,4] As most of the DWI and the DTI studies were performed with relatively low *b*-values ($b < 1500$ s mm^{-2}), only a single ADC was detected for water in neuronal tissues.

During the past few years several groups have shown that, at sufficiently high *b*-values, the water signal decay in diffusion experiments in neuronal tissues is not mono-exponential.[32–40] Once the experimental data cannot be analyzed by eqn. (1), it is necessary to decide on new approaches of analyzing the diffusing data. The different apparent components should then be assigned to real physical entities, if these components indeed represent such separate entities. Finally, verification should be attempted as to whether the different identified components provide more specific structural and physiological information concerning the investigated sample.

In this review, we will give a brief description of the **q**-space approach.[41,42] The recent applications of **q**-space diffusion MRS on biological samples in general, and of

CNS in particular, will then be described briefly, followed by the extension of this application to diffusion MRI. A few examples for the application of this approach for analyzing high *b*-value DWI data will be presented for demonstrating the potential of this approach in extracting structural and physiological information on neuronal systems. Examples both of high *b*-value **q**-space analyzed diffusion MR images of excised organs, where the short gradient pulse (SGP) approximation of the **q**-space theory can be met or approached, and of *in vivo* human studies, will be presented. Finally, a short discussion will deal with the potentials and limitations of the **q**-space approach in the context of high *b*-value DWI of neuronal tissues. The potential diagnostic capacity embedded in the apparent slow diffusing component will be discussed briefly at the end of this review.

High *b*-value diffusion-weighted MRS and MRI of water in neuronal tissues

Once the signal decay is not mono-exponential and eqn. (1) cannot be used to fit the data it seems that the simplest approach is to use a multi-exponential function as shown in eqn. (2)

$$E/E_0 = \sum_{i=1}^{n} A_i \exp[-\gamma^2 g^2 \delta^2 (\Delta - \delta/3)D_i]$$
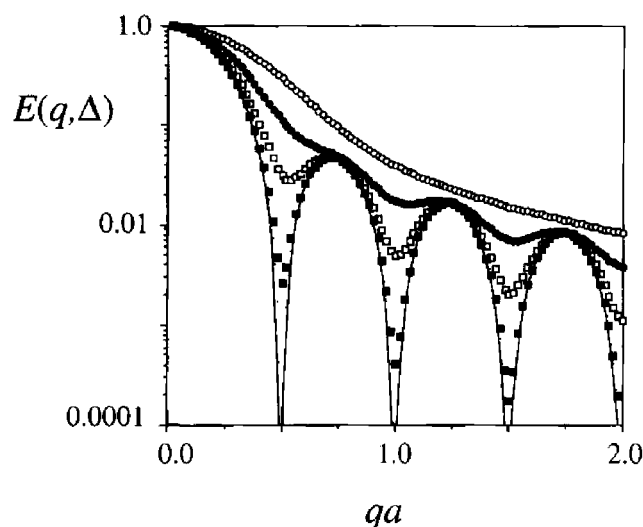$$= \sum_{i=1}^{n} A_i \exp(-bD_i) \quad (2)$$

In eqn. (2), A_i is the relative fraction of molecules having the diffusion coefficient D_i, n represents the number of components and all other parameters have the same meanings as in eqn. (1). However, it should be noted that the use of this equation implies the existence of several water populations that exhibit free diffusion and are in the slow exchange regime. Fitting the data with the simplest case of eqn. (2), i.e. a bi-exponential function, means that the system can be described by two free diffusing components with a slow exchange between them. Here, three independent parameters are used to obtain the fitting. Therefore, it is clear that the use of this fitting function is coupled to a certain model that does not necessarily describe the system accurately. However, the bi-exponential fit has been used more frequently, partially because the effect of exchange could be introduced to this model.[43] Until recently, most of the non-mono-exponential water signal decays in neuronal tissue were fitted with a bi-exponential function,[32–40] in analogy to what was proposed for water diffusion in cells.[44] It was therefore tempting to assign to the two major components to intra- and extracellular water. However, in some of these studies it was pointed out that the relative populations of the different components do not match those of the intra-

and extracellular spaces,[34] if one accepts the assumption that the low ADC of water should be attributed to water in the intracellular space. Others have used more elaborate models that include both exchange and geometrical factors of the systems.[35]

In addition, it is important to note that NMR diffusion experiments, such as the pulsed gradient spin-echo (PGSE), measure the mean displacement that the observed molecules perform during the diffusion time and not their diffusion coefficients *per se*. Therefore, to minimize the effect of restriction one should aim at performing diffusion measurements with very strong pulse gradients in which sufficient diffusion weighting is achieved when the gradient duration (δ) and the diffusion time (Δ) are both very short ($\sim$1 ms or less). For example, for a compartment of 2–4 μm and a self-diffusion coefficient of 1 mμ^2 ms^{-1} (1 $\times$ 10^{-5} cm^2 s^{-1}) the diffusion time should be significantly shorter than 2–8 ms, in order to minimize the effect of restriction. It should be noted that with such diffusion times the effect of exchange might also be largely suppressed. Under these experimental conditions, one may approach the situation in which differentiation between compartments based on the difference in their intrinsic diffusion coefficients is possible. There, the relative populations of the diffusing components should reflect the real populations of each compartment after correcting the signal intensity for relaxation effects (T_1 and, more importantly, T_2 effects). However, for extracting structural information from MR diffusion experiments, diffusion should be studied at the other extreme; namely, in the long diffusion time limit.[41,42] The long diffusion time limit is satisfied when $\Delta \gg a^2/2D$, where Δ is the diffusion time, D is the diffusion coefficient and a is the dimension of the compartment in which the diffusion takes place. At such a long diffusion time the molecules are able to explore the compartment in which they diffuse and hence their diffusion characteristics should, in principle, report on the compartment size and geometry. However, it should be noted that, under these experimental conditions, both restriction and exchange might be important, making the analysis of the diffusion data more complex. One way to analyze such data is to use the **q**-space analysis.[41,42]

q-Space analysis of NMR diffusion experiments

Since excellent comprehensive and authoritative reviews of the **q**-space theory of NMR diffusion experiments have appeared in recent years,[45,46] only a brief description addressing practical issues relevant to the specific application of **q**-space DWI in the CNS will be given here. As stated previously, in NMR diffusion experiments one tags the observed spins at two time points, and the echo decay in these experiments depends on the net displacement of the observed molecules during the
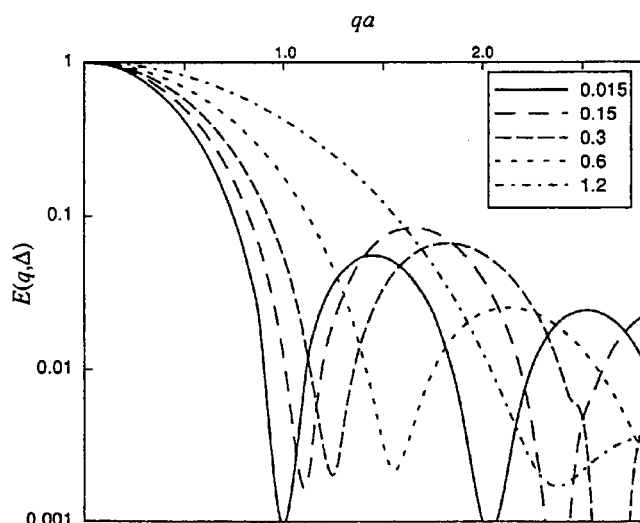

Figure 1. Simulated echo attenuation for spins trapped between parallel planes separated by a distance of 2a. Open circles represent data obtained with a diffusion time (Δ) of 0.2a^2/D; solid circles represent Δ of 0.5a^2/D; open squares represent Δ of 1.0a^2/D; solid squares represent Δ of 2.0a^2/D; and the continuous line represent infinite diffusion time (reproduced by permission of Academic Press from Callaghan[47])

diffusion time. Callaghan and his group demonstrated that, by using the 'reciprocal spatial vector', **q**, defined as $(2\pi)^{-1}\gamma\delta g$, instead of the b-value, it is possible to extract structural information on (pseudo)-periodic samples. According to this approach the echo attenuation in NMR diffusion experiments relates to the displacement probabilities, using the reciprocal spatial vector q according to eqn. (3),

$$E_\Delta(\mathbf{q}) = \int \overline{P}_s(\mathbf{R}, \Delta) \exp(i2\pi\mathbf{q} \cdot \mathbf{R})d\mathbf{R} \qquad (3)$$

where $E_\Delta(\mathbf{q})$ represents the echo decay as a function of **q**, **R** is the net displacement vector ($\mathbf{R} = \mathbf{r} - \mathbf{r}_0$), and $\overline{P}_s(\mathbf{R},\Delta)$ is the displacement probability. For molecules trapped in a compartment in which diffusion is restricted to a particular geometry (i.e. spherical, cylindrical) the displacement probability function may (at long Δ) relate to the size and shape of the compartment in which the diffusion occurs. These structural parameters will be reflected by diffraction peaks in the signal decay, as was predicted and found in porous materials.[47–49] Figures 1 and 2 show simulations of the signal decay $E(\mathbf{q})$ as a function of **q**a for diffusion between two perfectly reflecting rectangular barriers separated by a distance a. Pictorially, one can state that when a^2 is small compared to the distance that molecules having a diffusion coefficient, D, can travel during the diffusion time Δ, molecules will be 'reflected' from the barriers. Therefore, these molecules will have a greater probability of
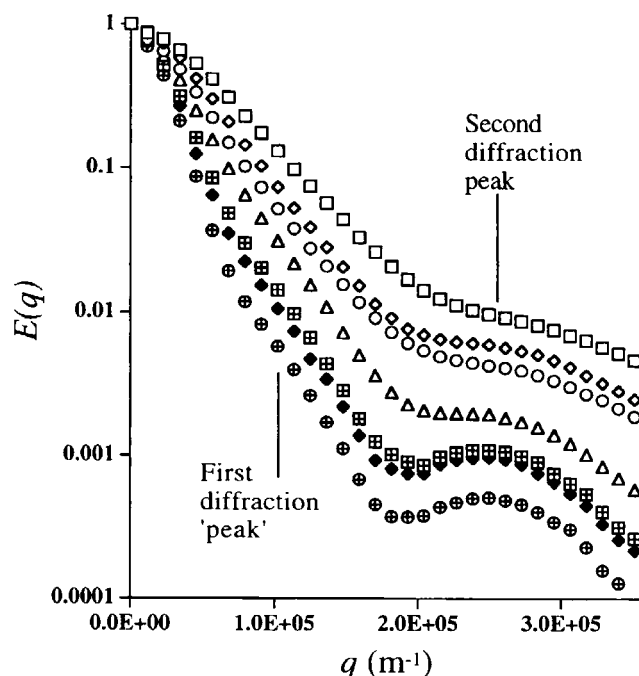
Figure 2. Echo attenuation calculated from Monte Carlo simulations for spins trapped between perfectly reflecting rectangular barriers. The line legends are for δ in a^2/D units. Note that as δ becomes bigger the diffraction peak moves to the right, meaning that the extracted distance for in between the plates becomes smaller. Reprinted with permission from Coy A, Callaghan PT. Pulsed gradient spin echo nuclear magnetic resonance of molecules diffusing between partially reflecting rectangular barriers. *J. Chem. Phys.* 1994; **101**: 4599–4609. Copyright 1994, American Institute of Physics

Figure 3. Diffusion signal decay curves for water in suspensions of human erythrocytes as a function of the **q**-value at different hematocrit. The hematocrit values are in decreasing order from the top of the figure, starting from a value of 93%, followed by 83, 73, 63, 47, 42, and ending at 25% at the bottom of the figure (reproduced by permission of Wiley-Liss, Inc. from Kuchel *et al.*[50])

returning to the position they occupied during the first pulse gradient. Consequently, the signal decay due to diffusion as a function of **q** will not decrease monotonically. As expected, the simulations in Fig. 1 show diffraction peaks and demonstrate that, when the diffusion time becomes shorter and Δ is no longer larger than $a^2/2D$, the diffraction peaks disappear.[47] These results demonstrate that, for obtaining structural information from NMR diffusion data the diffusion time, Δ, should be longer than $a^2/2D$.

Figure 2 shows simulations similar to those in Fig. 1. Here, the signal decay is plotted as a function of **q**a for different values of δ. This figure shows that, when the pulse gradient duration δ increases and the SPG approximation no longer holds, the diffraction peaks move to lower values of **q**a. Under these experimental conditions, the values that are extracted from the **q**-space analysis, values that should reflect the distance between the plates, become smaller. This means that for long δ the extracted dimensions extracted from the **q**-space analysis of NMR diffusion data are smaller than the real ones.[48]
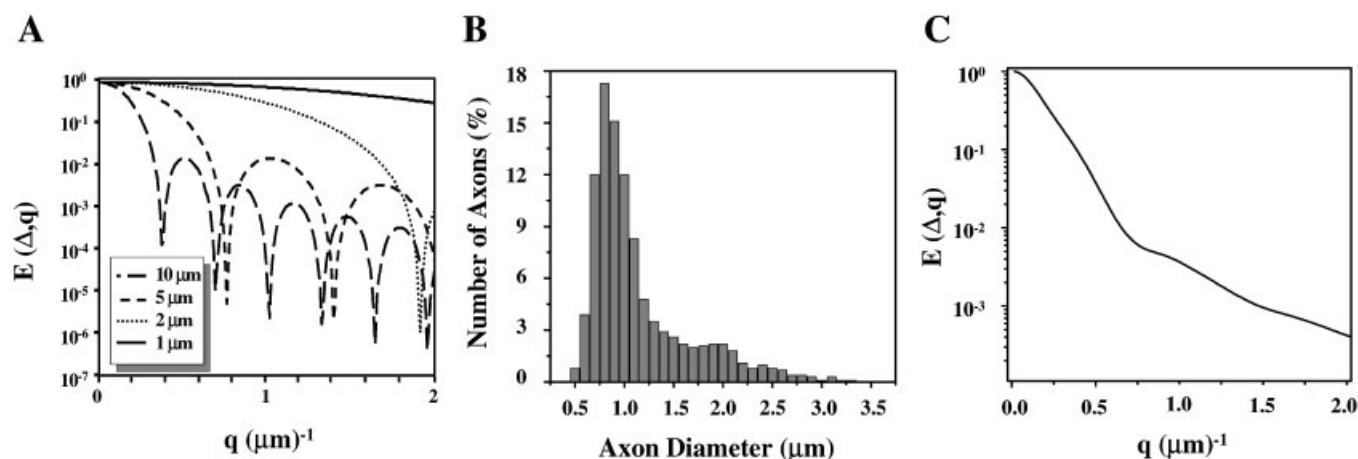
Kuchel and Stilbs have used **q**-space diffusion MRS to study the diffusion characteristics of red blood cells.[50] They observed the diffraction phenomena for water molecules in suspensions of red blood cells, which are relatively uniform in shape and size (Fig. 3).[50–52] Using intra- and extracellular (choline and phosphatidyl choline, respectively) markers, it was possible to assign the maxima and minima of the diffraction peaks to

restricted diffusion in the cells and to pore hopping in the extracellular space.[52] These experiments showed that even in biological systems that are known to be heterogeneous, structural information can be extracted, although the diffraction peaks were not as sharp as in porous materials, probably due to the effects of exchange and cell size variability. Subsequently, Kuchel showed, also by simulations, that when exchange is included the simulated curves showed much less pronounced diffraction peaks, which resembles the experimental curves.[53]

Peled *et al.* showed that when the sample is heterogeneous, consisting of cells of different sizes, even though they are all cylindrical, the diffraction phenomena vanishes.[54] In that case the decay curve approaches a multi-exponential decay curve. It was also found that the higher the **q**-values (or *b*-values) used in the diffusion experiment, the more exponents are apparent. Using Callaghan's formula for diffusion in cylindrical, spherical and planar geometries it is possible to simulate the signal decay for certain cell diameters.[47] Using this formula we produced the signal decay for ensembles of cylinders having different diameters, as shown in Fig. 4(A). In such simulations diffraction peaks that represent the diameter of the cylinder have been observed. Figure 4(C) shows the same simulation, but in this case for an ensemble of cylinders having the diameter distribution

Figure 4. (A) Simulated diffusion signal decay for diffusion in cylinders with different diameters, using the Callaghan formula[47] for diffusion perpendicular to the long axis of cylinders. (B) Axon diameter distribution taken from an electron-microscopy analysis of a squirrel's optic nerve.[55] (C) Simulated diffusion signal decay for diffusion in cylinders as in (A), but here the decay is calculated for an ensemble of cylinders having the diameter distribution shown in (B)

given in Fig. 4(B). It should be noted that the size distribution shown in Fig. 4(B) represents the axon diameter distribution as measured from histology of the squirrel optic nerve.[55] It is clear that the sharp diffraction peaks, which are clearly apparent when an ensemble of homogenous cylinders is considered, disappear when the decay curve is simulated for an ensemble of cylinders of different sizes. In such a case, when no diffraction peaks are observed, it seems that it is much more difficult to extract structural information from the signal decay.
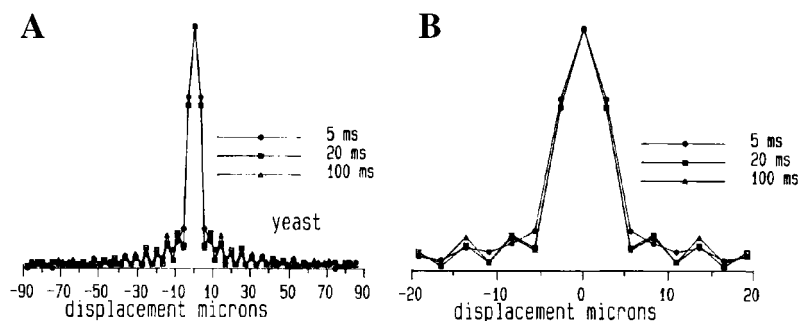
In 1990, Cory and Garroway utilized the Fourier relation between the decay of the echo intensity, $E_\Delta(\mathbf{q})$, and the displacement probability, $\overline{P}_s(\mathbf{R},\Delta)$ to extract structural information on an heterogeneous systems from such diffusion experiments.[41] They used yeast cells to show that, by Fourier transformation of the signal decay, it is possible to extract the displacement distribution profile which give, under the SGP condition, the cells' diameter as shown in Fig. 5. In that article, Cory and Garroway developed the **q**-space analysis mathematically for displacement distributions having a Gaussian shape.[41] From the distribution profile, both the diffusion

coefficient, D, and the root mean square displacement (ΔX_{rms}), could be calculated from the full-width at half-height of the displacement distribution function ($\Delta X_{0.5}$) using eqns (4) and (5), in which t_d is the diffusion time.
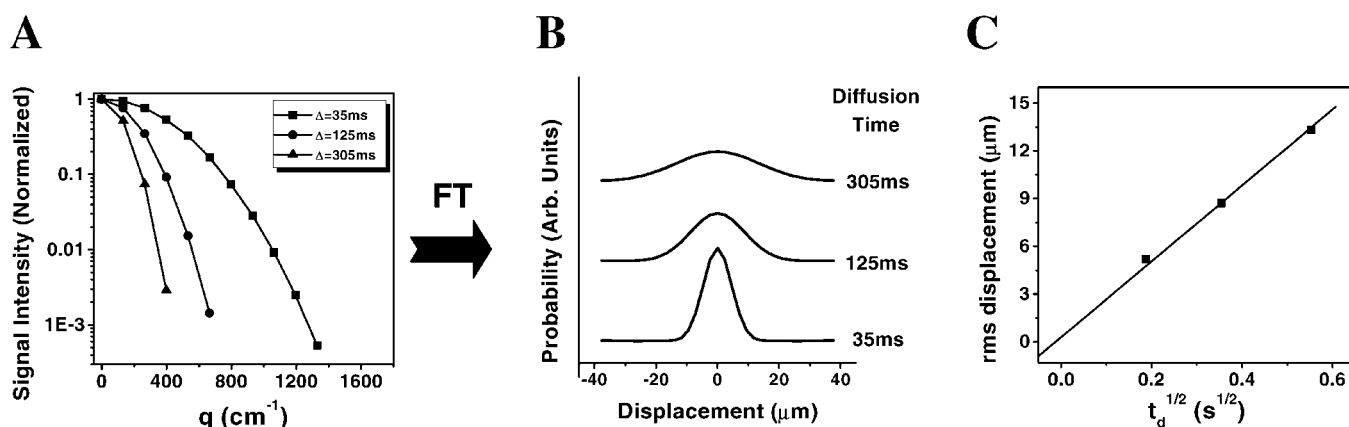
$$\Delta X_{0.5} = 2[4D \ln t_d 2]^{1/2} \quad (4)$$

$$\Delta X_{rms} = [2D t_d]^{1/2} = 0.425 \Delta X_{0.5} \quad (5)$$

Figure 6 shows the **q**-space analysis, as developed by Cory and Garroway, for an isotropic solution of *t*-butanol. Figure 6(A) shows the experimental signal decay of *t*-butanol at different diffusion times. Figure 6(B) shows the effect of the diffusion time on the displacement distribution profiles obtained by Fourier transformation of the data shown in Fig. 6(A). The data in Fig. 6 show that, as the diffusion time increases, the *t*-butanol molecules can travel greater distances and the probability for zero displacement decreases. Using eqn. (4) one can relate the displacement profile to the diffusion coefficient. In order to do that, one has to acquire the signal decay until it reaches less than 1% of its original value and to plot it on a logarithmic scale as a

Figure 5. Displacement distribution profile for water diffusion in yeast cells at diffusion times of 5, 20 and 100 ms. (B) is an expansion of (A) (reproduced by permission of Wiley-Liss, Inc. from Cory and Garroway[41])
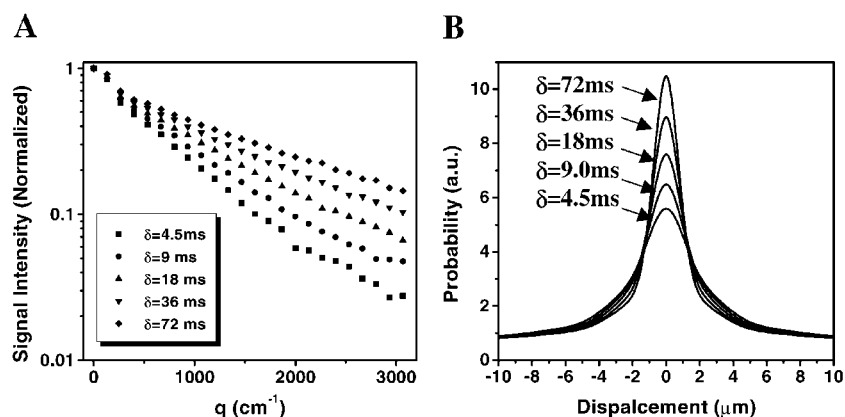
A

B

C

Figure 6. (A) Signal decay in PGSE experiment of *t*-butanol at 25 °C at three diffusion times of 35, 125 and 305 ms. (B) Displacement distribution profiles calculated by Fourier transformation of the data shown in (A). (C) The rms displacement calculated from the full-width at half-height of the Gaussian displacement distribution profiles shown in (B) against the square root of the diffusion time. The slope of the straight line in (C) provides the self-diffusion coefficient of *t*-butanol (2.7×10^{-6} cm^2 s^{-1}) (reproduced by permission of Wiley-Liss, Inc. from Assaf and Cohen[66])

function of the **q**-values [Fig. 6(A)]. The displacement distribution profiles can be produced by Fourier transformation of the signal decays in Fig. 6(A) for each diffusion time [Fig. 6(B)]. The full-width at half-height ($\Delta X_{0.5}$) is then used to calculate the root mean square displacement (ΔX_{rms}) from these profiles for each diffusion time. The slope of the plot of ΔX_{rms} as a function of the square root of the diffusion time [Fig. 6(C)] is then proportional to the diffusion coefficient of the diffusing molecules. Indeed, when this approach was performed for a solution of *t*-butanol it was possible to extract from the slope of the graph in Fig. 6(C) the actual self-diffusion coefficient of *t*-butanol. Therefore, for the case of isotropic diffusion one can relate the displacement profile and the diffusion coefficient using eqn. (4). In cases of non-Gaussian diffusion, as is found in biological tissues, one can use this relation to calculate the apparent diffusion coefficient (ADC) if a mono-exponential signal decay is observed. The comparison between Figs 5(B) and 6(B), which show the effect of the diffusion time on the displacement profiles for restricted and un-restricted diffusion modes, demonstrates the power of this approach for recognizing restricted diffusion. In the case where restriction is significant, the increase in the diffusion time does not result in a wider displacement distribution profile.

q-Space analysis and experimental parameters

The **q**-space analysis provides a means of obtaining displacement–probability profiles even in complex systems by performing a Fourier transformation of the echo decay with respect to **q** even when diffraction peaks are not observed. This means that **q**-space analysis of MR diffusion experiments is suitable for obtaining structural information on the investigated sample, non-invasively.

However, as stated previously, the **q**-space analysis was developed under the short gradient pulse (SGP) approximation, i.e. for cases in which $\delta \rightarrow 0$ and $\delta \ll \Delta$. However, in many cases the SGP approximation is violated due to insufficient strength of the pulsed gradients, which requires the use of long gradient pulses in order to achieve adequate *b* or **q** values. The effect of long gradient pulses was investigated theoretically by simulations[48,56] which predicted that the measured cell size would be smaller than the real size when the SGP condition is violated. Since, in neurological systems, factors other than restriction may influence the signal decay (i.e. compartmentation, exchange) we studied the effect of the pulsed gradient length (δ) on the signal decay and the displacement distribution profiles, experimentally. Figure 7(A) depicts the normalized signal decay of water in excised sciatic nerve for a series of diffusion experiments where both δ and g were varied in a way that kept the **q** values (and *b*-values) the same in all experiments. Figure 7(B) shows the displacement distribution profiles obtained by FT of the decay curves shown in Fig. 7(A). In these experiments, we started with a combination of δ and g_{max} of 4.5 ms and 160 Gauss cm^{-1}, respectively, for which the mean displacements extracted from the **q**-space analysis were found to be in good agreement with the axons size distribution observed by EM (see below).[57] For extreme violation of the SGP condition we used the following parameters: $g_{max} = 10$ Gauss cm^{-1} and $\delta = 72$ ms, which approaches the experimental parameters used in the clinical set-up of such diffusion experiments (see below). In these experiments all other experimental parameters were kept constant (*TR*, *TE*, **q**-value, *b*-value, Δ). The data in Fig. 7(A) shows that, as expected for restricted diffusion,[48,56] the signal decay becomes smaller when the diffusion gradient duration, δ, is increased and the apparent relative

A   **B**

Figure 7. The effect of the length of the diffusion gradient pulse (δ) on the water diffusion in sciatic nerve. (A) Effect on the signal decays. (B) Effect on the respective **q**-space distribution profiles. The gradients were applied perpendicular to the long axis of the nerve. Diffusion experiments were performed on an 8.4 T NMR spectrometer equipped with a micro5 gradient probe driven by a BGU-II system producing pulse gradients of up to 190 Gauss cm^{-1} in each of the three directions. Diffusion experiments were performed using the PGSE pulse sequence with the following parameters: *TR/TE* = 3000/206 ms and $\Delta = 100$ ms. Five sets of experiments were performed with different diffusion gradient duration and amplitude and 24 data points but with the same **q**- and *b*-values. The duration of the diffusion gradients was 4.5, 9, 18, 36 and 72 ms with respective gradient amplitudes of 160, 80, 40, 20 and 10 Gauss cm^{-1} (reproduced by permission of Wiley-Liss, Inc. from Assaf *et al.*[89])
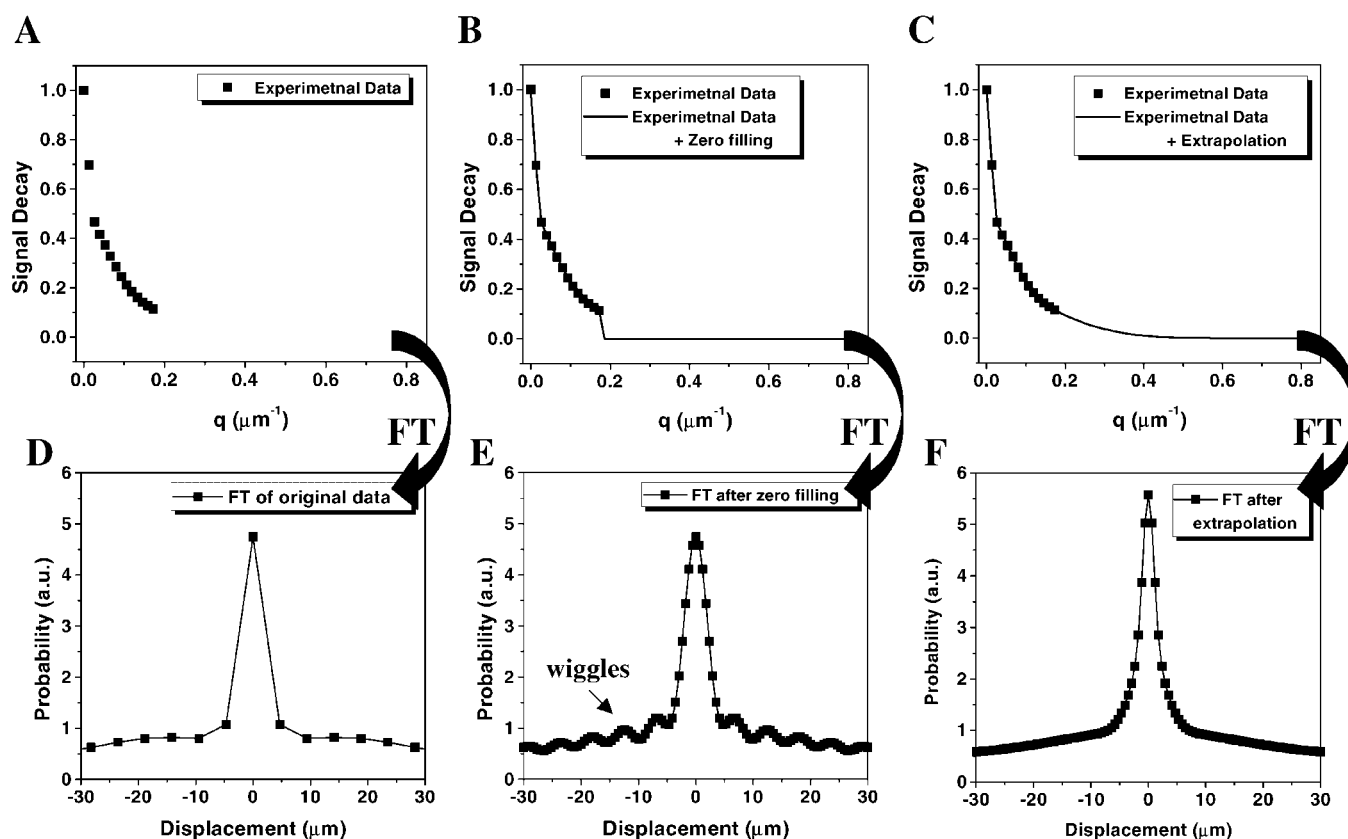
population of the slow diffusing component becomes larger. Consequently, the extracted displacement distribution profiles become narrower and more intense.[58] These results show that the displacement extracted from the **q**-space analysis of these diffusion data decreased from a value of 3.3 μm at δ of 4.5 ms to a value of about 1.6 μm at δ of 72 ms. This implies that, when one is forced to use long δ, as on clinical MRI scanners, the mean displacements obtained from the **q**-space analysis are smaller than the physical size of the compartment in which the restricted diffusion takes place. However, the differences are not very large and, even when δ is changed by a factor of 16, the extracted mean displacements vary only by a factor of two.[58] Thus, the utilization of long diffusion gradient pulses overemphasizes the restricted component. This experiment suggests that, when extracting an ADC from diffusion experiments in which the diffusion is restricted, the ADC depends not only on the diffusion time but also on the pulsed gradient strength. In this case, it might be possible that for two equivalent *b*-values, one having short gradient pulse and strong gradient strength and the other having a long gradient pulse and small gradient amplitude, two different ADC values will be calculated. These results demonstrate that, in general, caution should be exercised when comparing ADCs obtained from different experiments performed with different experimental parameters. Regarding the structural parameter obtained from a **q**-space analysis when the SGP approximation is violated, it should be noted that the extracted absolute numbers might be not

very accurate. Nevertheless, their relative size extracted from such a **q**-space analysis will reflect the relative physical sizes of the different compartments.

Besides the need to perform the diffusion experiment over a long diffusion time scale and under short-pulse-gradient conditions, in order to extract the real dimensions of the compartment in which the diffusion occurs, adequate spatial resolution should be used. The spatial resolution of the **q**-space analysis is determined by the maximal magnitude of the pulsed gradients or the maximal **q**-value that is used in the measurements ($\mathbf{q}_{max}$). In the yeast cells example (Fig. 5) the resolution was 2.75 μm[41] (distance between two adjacent point in the **q**-space profile), while in the mouse brain example the resolution was 4.1 μm (see below).[59,60] In principle, the spatial resolution can be calculated using eqn. (6):

$$R = \frac{1}{N \cdot \Delta \mathbf{q}} \tag{6}$$

where R is the resolution, N is the number of gradient points acquired in the PGSE experiment and $\Delta\mathbf{q}$ is the difference in **q**-values between two adjacent gradient points (assuming that the **q**-values are changed linearly and are equally spaced). A gradient system with a maximal gradient amplitude of 100 G cm^{-1} and 2 ms gradient pulse duration will give a displacement resolution of about 11 μm. This resolution is insufficient to measure displacements in biological systems in which the cell sizes may be of 5 μm or less.

Figure 8. Increasing **q**-space resolution using zero filling (zf) and data extrapolation. (A) Original data and (D) the Fourier transformation (FT) of the data in (A). (B) Original data and the zero filled curve and (E) the corresponding displacement profile obtained by FT of the data in (B). Notice that zero filling produces wiggles in the displacement distribution profile, due to the truncation of the data. (C) Original data and the extrapolated curve and the corresponding displacement profile (F) obtained by FT of the data in (C). The resolution is 5.8 μm in (D) and 0.6 μm in (E) and (F)
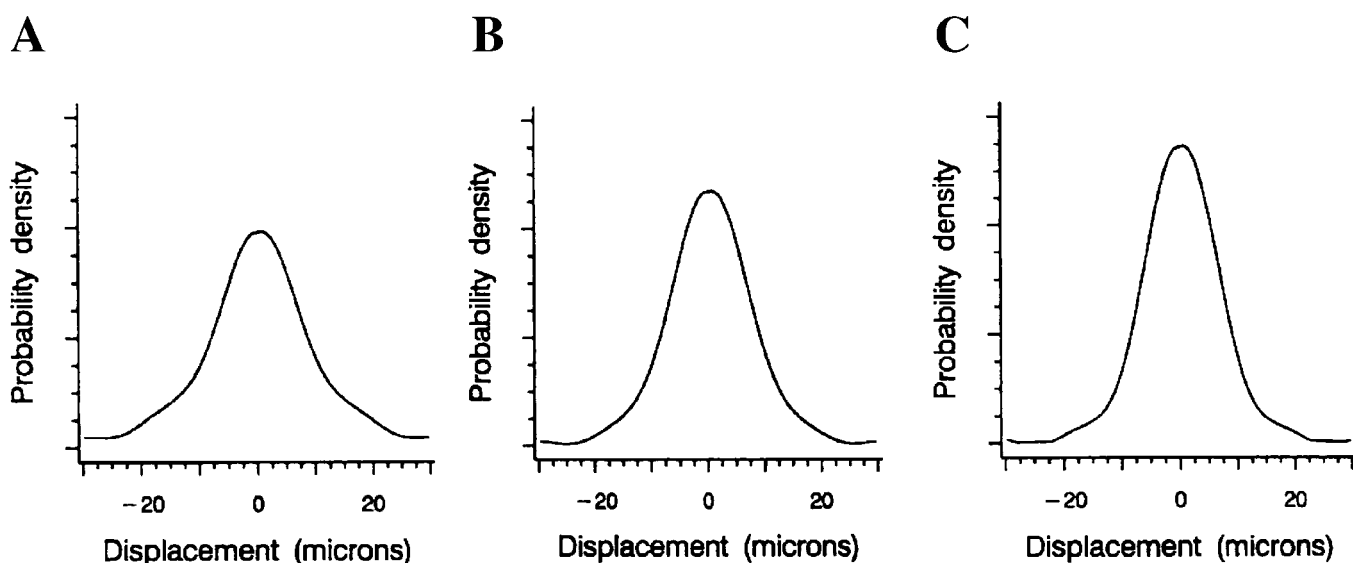
In principle, there are two ways to increase the spatial resolution of the Fourier transformation: zero filling and data extrapolation to higher **q**-values, as shown in Fig. 8. Enhancement of the resolution by zero filling or extrapolation allows extraction of smaller displacement, even though the hardware limits the resolution. Zero filling is a less subjective method for resolution enhancement and is commonly used when the signal decays to less than 2–4% of its original value at q_{max}. In cases where the signal decays to higher values (>4% of its original value) zero filling will result in wiggles in the displacement probability profile, as shown in Fig. 8(E). In these cases, data extrapolation seems to be the better choice, compared with zero filling. However, it should be noted that extrapolation requires fitting the data to a model, the accuracy and validity of which may be questioned.

q-Space diffusion MRS in neuronal tissues

King *et al.* were the first to use the **q**-space approach on neuronal tissues.[59,60] They used the displacement distribution profile to calculate the fraction of water molecules that exhibits a net displacement of less than 10 μm in normal, ischemic and postmortem brain tissues using localized diffusion spectroscopy (Fig. 9).[59,60] They found that in ischemic or postmortem conditions the displacement distribution profile becomes narrower, which is consistent with the ADC reduction observed after stroke.[59,60] They also found that in ischemic, and even more so in postmortem, conditions the fraction of water molecules having a mean displacement of less than 10 μm increases. In their second article,[60] King *et al.* discuss the possible causes for the existence of non-mono-exponential decay curves. They attributed the non-gaussian behavior of the decay curves to tissue heterogeneity and restricted diffusion in the region of interest. Despite this heterogeneity and the non-gaussian decay curves, it is interesting that in these studies a nearly mono-gaussian displacement distribution profile was observed, which in turn was attributed to the large heterogeneity of the examined ROI and to the effect of exchange. These studies demonstrated that there is a significant water component that persists even at high diffusion weighting, implying a water population with an
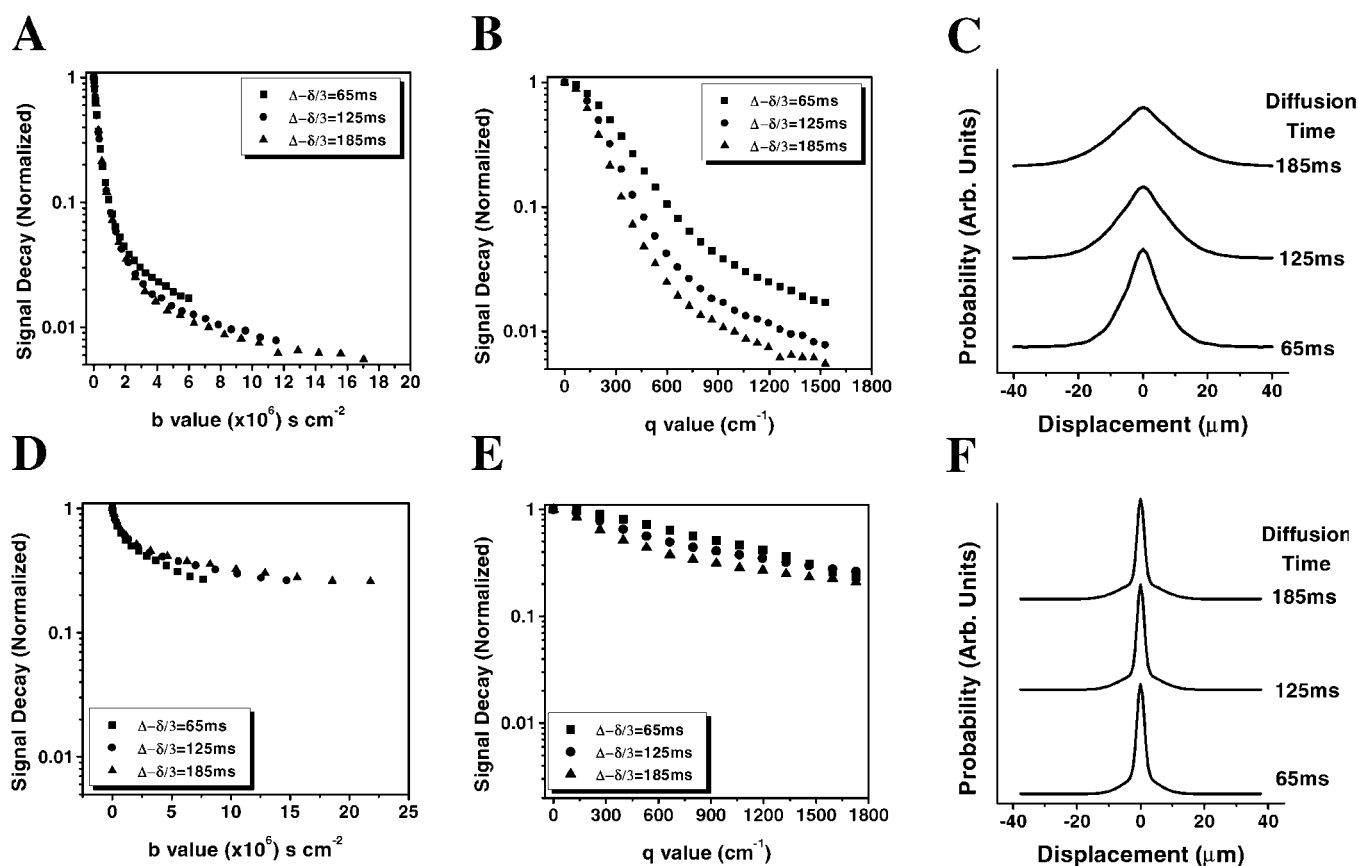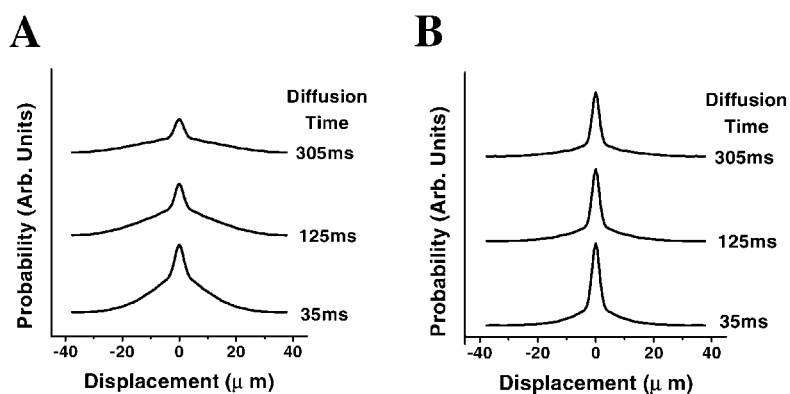
A

B

C

Figure 9. Water displacement profiles derived from **q**-space measurements for (A) intact, *in vivo* mouse brain, (B) ischemic lesion in an *in vivo* mouse brain and (C) post-mortem, *in situ* mouse brain (reproduced by permission of Wiley-Liss, Inc. from King *et al.*[60])

apparent slow diffusion coefficient. Although their studies could not shed light on the origin of the low ADC in ischemic brain tissues, they did demonstrate that

some structural (although limited) information could be obtained from the **q**-space analysis of such diffusion data.

A

B

C

D

E

F

Figure 10. Water signal decay curves in diffusion experiments on excised rat brain at different diffusion times as a function of (A) the *b*-values, and (B) the **q**-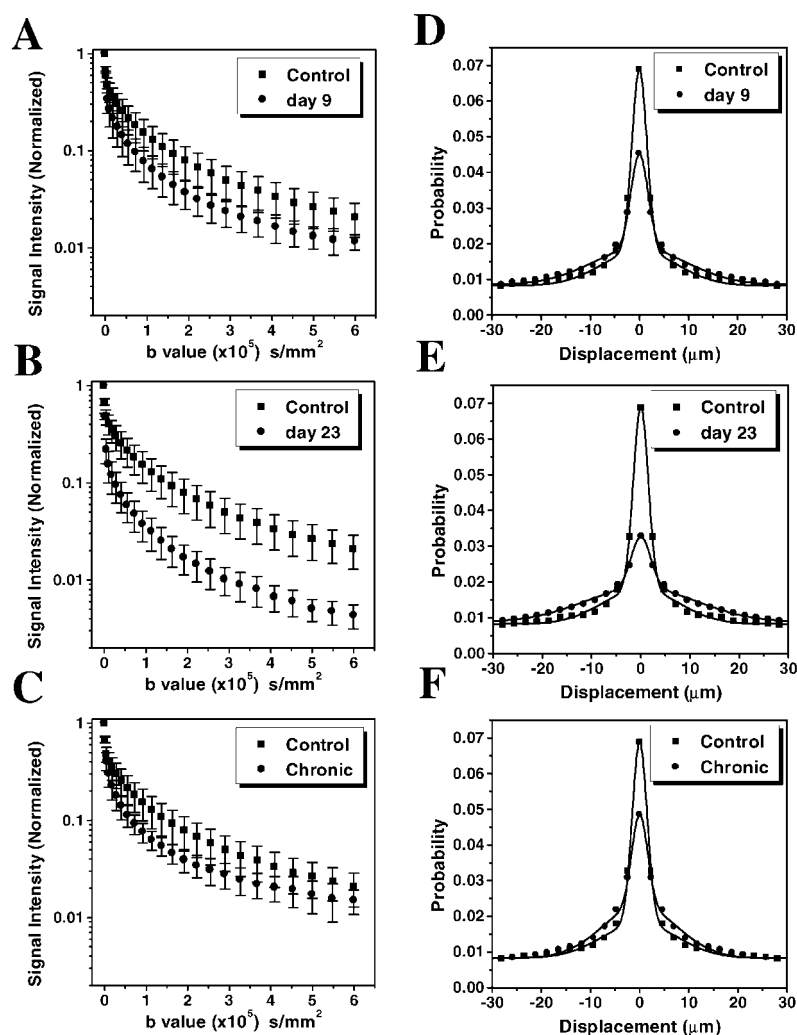values. (C) The respective displacement profiles of the data shown in (B). NAA signal decay in diffusion experiments performed on excised rat brain at different diffusion times as a function of (D) the *b*-values, and (E) the **q**-values. (F) The respective displacement profiles of the data are shown in (E)

Figure 11. Displacement distribution profiles from (A) excised bovine optic nerve measured parallel to the long axis of the nerve and (B) excised bovine optic nerve measured perpendicular to the long axis of the nerve. The data was acquired on an 11.7 T spectrometer with a *z*-gradient probe. The stimulated echo diffusion pulse sequence was used with the following parameters: $TR/TE = 3000/70$ ms, $\delta = 15$ ms, $g_{max} = 27$ g cm^{-1} and $q_{max} = 1727$ cm^{-1}.[66]

As of 1996 we were interested in finding a probe that would allow cell swelling to be measured in neuronal tissue non-invasively.[61] Therefore, we looked for a cellular marker that would report on the size of the compartment. Water is found in all compartments and is generally known to exchange across membranes faster than metabolites.[62,63] Indeed, King *et al.* have noted that, during the diffusion time of 50 ms that was used in that study, the majority of the water molecules have diffused over a distance greater than three times the cell spacing, probably due to fast exchange between intra- and extra-cellular spaces.[60] Therefore, to minimize the effect of exchange, we decided to study the diffusion characteristics of intracellular metabolites at high *b*-values and long diffusion time, first using a multi-exponential model and later using the **q**-space approach.[62–64] Figure 10(A) and 10(B) shows the water signal decays as a function of the *b* and **q**-values, respectively while Fig. 10(C) shows the respective displacement distribution profiles for water in excised rat brain at different diffusion times. The displacement distribution profiles shown in Fig. 10(C) were obtained by FT of the data shown in Fig. 10(B). Figures 10(D), 10(E) and 10(F) show the same data set obtained with the same experimental parameters, on the same samples but for N-acetyl aspartate (NAA). Interestingly, the effect of diffusion time on the decay curves of water and NAA as a function of the *b*-values was very different. For water molecules, it was found that as $(\Delta - \delta/3)$ increased the apparent fraction of the slow diffusing component decreased, while the opposite trend was observed for the NAA molecules. This is to be expected, since in the water case, exchange is probably more important than restriction, while in the NAA case it seems that restriction is the dominant factor.[64] When the water and the NAA signal decays are plotted against the **q**-values for different diffusion times, one can observe

that the diffusion time has a larger effect on the water decay curves. However, the interesting point is the effect of the diffusion time on the displacement distribution profiles. With the increase in the diffusion time the water displacement profiles become wider, indicating that the water molecules translate larger distances as the diffusion time increased, exhibiting almost free diffusion. In the NAA case, however, the displacement profiles are almost the same at the different diffusion times, suggesting that the diffusion of this fraction of metabolites is highly restricted. These results imply that structural information about the intracellular compartment could be obtained from diffusion characteristics of metabolites.[36,61–64] However, when high *b*-values water diffusion in optic nerve was studied by the **q**-space approach the existence of a large water population that exhibits restricted diffusion was found as shown in Fig. 11.[65,66] Interestingly, it was found that the effect of diffusion time on the water signal decay, as a function of the *b*-values in the in optic nerve and in brain tissues, shows opposite trends. In nerve, the water signal decay as a function of the diffusion times behaves similarly to the signal decay of the metabolites in brain tissues (where exchange effects are less important). Figures 10(C) and 11, showing the displacement distribution profiles of water in brain tissues and in bovine optic nerve in two orientations [Fig. 11(A) and 11(B)] for different diffusion times, demonstrate the ability of the **q**-space analysis to identify restricted diffusion. In the isotropic solution of tert-butanol, a gaussian distribution profile is obtained [see Fig. 6(B)] and the mean displacement increases linearly with the square root of t_d [Fig. 6(C)], as expected from eqn. (4). For water in nerve, however, it is clear that in both orientations there is a component for which the displacement distribution profile is not affected by the increase in the diffusion time as expected for restricted
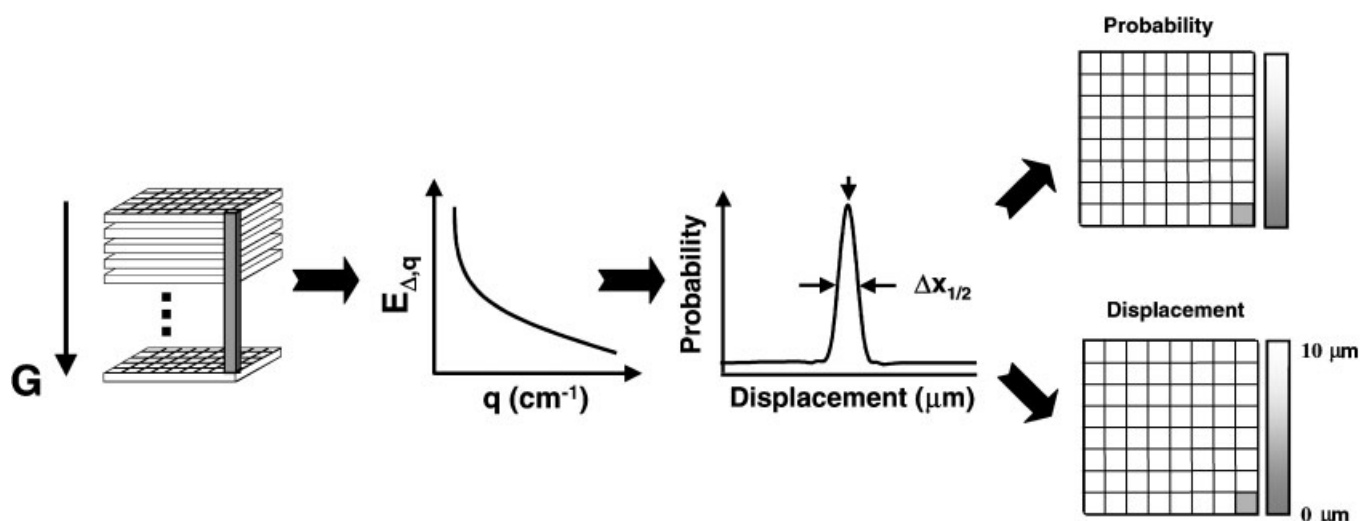
Figure 12. Water signal decay in diffusion experiments and the respective **q**-space profiles for control and EAN diseased sciatic nerves. Normalized signal intensities for (A) day 9, (B) day 23 post-immunization and (C) for the chronic phase groups along with the signal intensity of the control group. Displacement distribution profiles for (D) day 9, (E) day 23 post-immunization and (F) for the chronic phase groups along with the **q**-space profile of the control group.[67]

diffusion [Fig. 11(A) and (B)].[65,66] When the diffusion is measured perpendicular to the fibers' direction in the nerve, the relative weighting of the restricted component is even larger [Fig. 11(B)]. In the nerve experiments, in which diffusion was measured parallel to the long axis of the nerve, mixed behavior was detected; whereas the narrow component was not influenced by the diffusion time, the displacement of the broad (fast) component became larger as the diffusion time increased. A close examination of the displacement distribution profile reveals that, even in brain tissue, there is a small component for which the mean displacement does not increase linearly with the square root of the diffusion time.[65,66]

The results shown in Figs 10(C) and 11 demonstrate

that a certain fraction of water molecules are restricted to a compartment of about $2\,\mu m$. More importantly, although the compartment size in which the restricted diffusion occurs seems to be very similar for the different CNS tissues, the relative weighting of this restricted component is larger in white matter-rich areas and depends on its orientation.[66] These observations suggest that this slow and restricted diffusing component is much more prominent in white matter.[64–66] Therefore, it was postulated that water diffusion at high b-values and long diffusion time (and relatively long TE) may provide a useful means for following the pathophysiological state of white matter.

Diffusion in the axonal milieu is one possible explanation for the slow restricted diffusing component.

Figure 13. The steps for obtaining **q**-space analyzed MR images for system in which the direction of the fiber is known *a priori* and the diffusion needs to be measured only in one direction (perpendicular to the long axis of the fibers).[68]
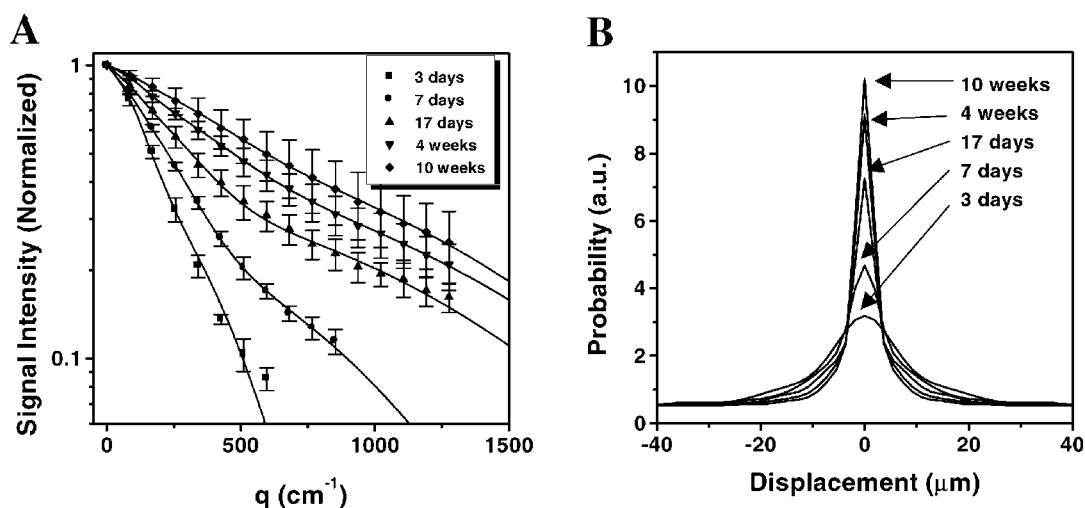
If this assignment is correct, any process of demyelination should have a strong effect on the weighting and on the diffusion characteristics of this slow component observed at high diffusion weighting. Therefore it seems logical to study experimental allergic neuritis (EAN) using high-*b*-value **q**-space DWI since it is as an animal model where demyelination occurs.[57,67] In this model, rats are immunized with myelin basic protein, which causes an autoimmune reaction against myelin that results in progressive demyelination on the peripheral nervous system (PNS). In the chronic stages of this model, remyelination occurs. In the peripheral sciatic nerve, a multi-exponential signal decay was also observed, as in the cases for CNS tissues [Fig. 12(A)]. In this study the signal of water in the sciatic nerves could not be fitted accurately even by a bi-exponential function. Only a tri-exponential function gave a good fit to the experimental data, motivating us to use **q**-space analysis in this study also.[67] Indeed, the results were as expected. It was found that the weighting of the slow diffusing component decreased significantly with the progression of demyelination and increased, although not to control values, when remyelination occurred [Fig. 12(A–C)]. The **q**-space profiles obtained by FT of the data shown in Fig. 12(A–C), enabled characterization of these changes, as shown in Fig. 12(D–F). These figures show a decrease in the population of the component with the narrow displacement profile and an overall broadening of the displacement profile following induction of the EAN. It was found that the weighting of the slow diffusing component that is restricted decreased by 20% between control and EAN diseased sciatic nerves at day 9 post-immunization. Concomitantly, the mean displacement of the restricted component increased by 33% from a value of $3.9 \pm 0.4 \, \mu m$ for control nerves to a value of $5.2 \pm 0.1 \, \mu m$ for diseased nerves.[67] The high *b*-value **q**-space MRS was able to detect the EAN pathology at day 9 [Fig. 12(A) and 12(D)] before the appearance of any clinical signs. In addition, both the deterioration up to day 23 post-immunization, the time at which maximal demyelination occurred [Fig. 12(B) and (E)], and the improvement at the chronic stage [Fig. 12(C) and (F)], could be followed using **q**-space diffusion MRS. The structural changes correlated well with electron microscopy.[67]

All these recent applications of **q**-space diffusion in biological samples dealt with diffusion-weighted MRS and, as such, gave only average values for the entire system.[41,50–53,57,59,60,64–67] Biological systems are heterogeneous in nature and it is therefore desirable to obtain the spatial distribution of the parameters extracted from the **q**-space analysis for each pixel. We therefore computed displacement and probability MR images or maps based on the **q**-space analysis of high *b*-value DWI. These images were used to study the pathophysiological state of white matter.[68]

q-Space displacements and probabilities MR images

The procedure for obtaining the **q**-space MR images was described previously and is outlined schematically in Fig. 13.[68] In principle, a set of diffusion images is arranged in a 3D array in which the *x* and *y* coordinates are the image axes and the *z* direction is that of the **q**-values. The *z* direction is then zero-filled (in some cases, for comparison the *z* direction was extrapolated using a multiexponential decay function) in order to increase FT resolution. Then the signal decay in each pixel of the image was transformed into displacement distribution profiles using eqn. (3) by an in-house Matlab® program.

Figure 14. The effect of spinal cord maturation on (A) the white water signal decay with respect to **q**, and on (B) the respective displacement distribution profiles obtained by FT of the data shown in (A). Data obtained when diffusion was measured perpendicular to the long axis on the cord and with a diffusion time of 150 ms. The data were acquired on a Bruker 8.4 T spectrometer equipped with a micro-imaging accessory. The stimulated echo diffusion pulse sequence was used with the following parameters: TR/TE = 1500/30 ms, Δ/δ = 150/2 ms, g_{max} = 150 g cm^{-1} and q_{max} = 1277 cm^{-1}.[68]

The Fourier transformation of the signal decay with respect to **q** produced a non-mono-gaussian displacement–distribution profile for each pixel in the image. In the spinal cord, diffusion was measured perpendicular to the long axis of the fibers of the spinal cord, resulting in only one displacement distribution function for each pixel. Two parameters of the displacement distribution profile, namely the displacement as calculated from the full width at half-height and the probability for zero displacement (given by the height of the displacement profile at zero displacement), are then extracted for each pixel. Finally, two sub-images based on these two parameters are constructed on a pixel-by-pixel basis.
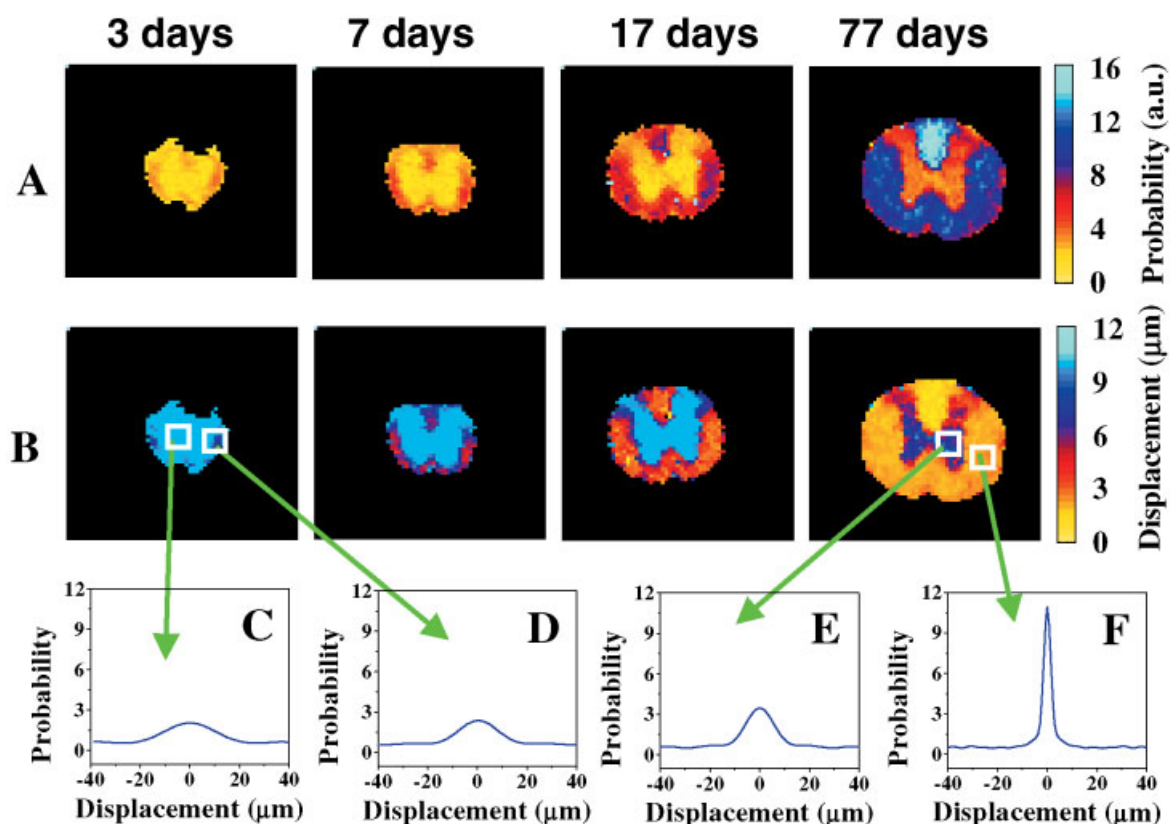
APPLICATION OF HIGH *b*-VALUE q-SPACE DWI

As stated previously, the data in Fig. 11 imply that there is a large fraction of water molecules in optic nerve whose diffusion is restricted to about 2 μ, even when the MR diffusion experiments were carried out with a diffusion time of 305 ms.[65,66] These studies also showed that this slow diffusing population is much larger in white matter than in gray matter and it was found that the displacement of this component hardly changes when the diffusion time is increased by a factor of about 10.[65] It was also found that, in optic nerve, the relative fraction of the apparent slow diffusing component depends strongly on the relative orientation of the diffusion-sensitizing gradients with respect to fiber orientation.[65,66] Based on these findings we suggested that axonal water contributes significantly to this apparent slow-diffusing compo-

nent.[65,66] This conclusion was the driving force for the attempts to evaluate the diagnostic capacity embedded in this apparent slow-diffusing component. Both white matter maturation and degeneration as well as spinal cord trauma were evaluated first by high *b*-value **q**-space DWI.[68,69,72]

High *b*-value q-space DWI of *in vitro* spinal cord maturation

One of the first models that was used to test the high *b*-value **q**-space DWI approach was spinal cord maturation in the rat.[68] Figure 14(A) shows the effect of the spinal cord maturation on the water signal decay as a function of *q* and Fig. 14(B) shows the respective displacement–distribution profiles obtained by FT of the decay curves shown in Fig. 14(A) after extrapolation. This figure clearly demonstrates that, as maturation progresses, the displacement–distribution profile becomes narrower and more intense, indicating an increase in the component of spinal cord water that exhibits restricted diffusion.[68] **q**-Space analyzed MR images that follow the spinal cord maturation are shown in Fig. 15. This Figure shows the displacement and probability MR images of spinal cords of rats at ages of 3, 7, 17 and 77 days taken with a diffusion time of 150 ms. The mean displacement of the water molecules in the white matter decreased with age, reaching a value of about 2.2 ± 0.3 μm at 77 days. At 3 days, the mean displacement in the white matter was similar to that in the gray matter (9.6 ± 0.2 and 9.8 ± 0.2 μm, respectively). Significant changes were also observed in the probability images. Here it was

Figure 15. (A) **q**-Space displacement and (B) probability MR images of spinal cords of rats of different ages along with the displacement distribution profiles of the ROIs depicted on the images. (C) and (D) show the displacement profiles of gray and white matter of 3-day-old rat spinal cord, respectively, and (E) and (F) show the profile in the gray and white matter of a mature rat spinal cord, respectively. For experimental details see Fig. 14 (reproduced by permission of Wiley-Liss, Inc. from Assaf *et al.*[68])
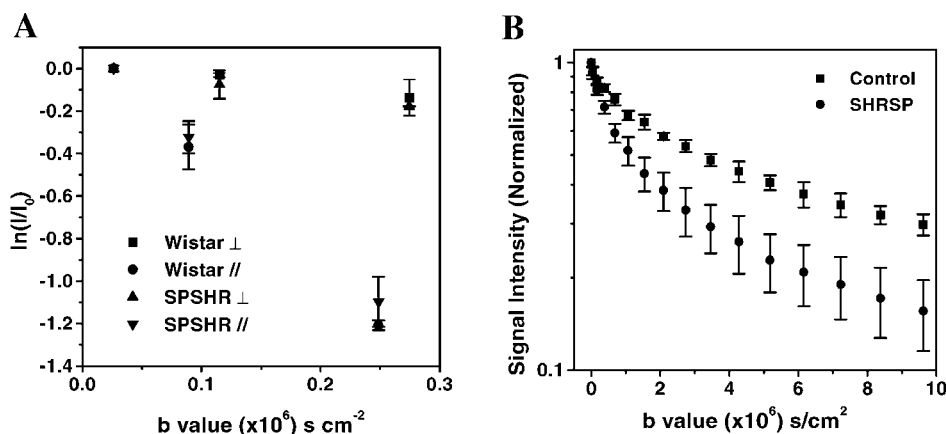
found that the probability of zero displacement increased with age. Analysis of the pixels in the white and gray matter of the newborn and mature rat spinal cords revealed that the contrast is formed due to the change in the diffusion characteristics of the white matter upon maturation.[68] As seen in Fig. 15, the mean displacement in the gray matter barely changed between day 3 [Fig. 15(C)] and day 77 [Fig. 15(E)]. It is the dramatic decrease in the mean displacement in the white matter, from 9–10 μm [Fig. 15(D)] to around 2–3 μm [Fig. 15(F)], which brings about the formation of the gray–white matter contrast in the mature spinal cord. This data shows that the progression of maturation, which is also accompanied by myelination, brings about the restriction observed in the mature white matter.

High *b*-value q-space DWI of spinal cord degeneration caused by chronic hypertension[69]

It is well known that chronic hypertension (high blood pressure) is one of the major risk factors for ischemic white matter lesions (also termed leukoaraiosis) or vascular dementia (VaD).[70,71] Some of the clinical signs

following VaD seem to be related to the progression of demyelination and axonal loss. It is known that stroke-prone spontaneous hypertensive rats (SP-SHRs) develop, under a high-salt diet, chronic hypertension that may lead to multi-focal stroke lesions in the brain, which in turn can lead to neuronal degeneration, even in the spinal cord.
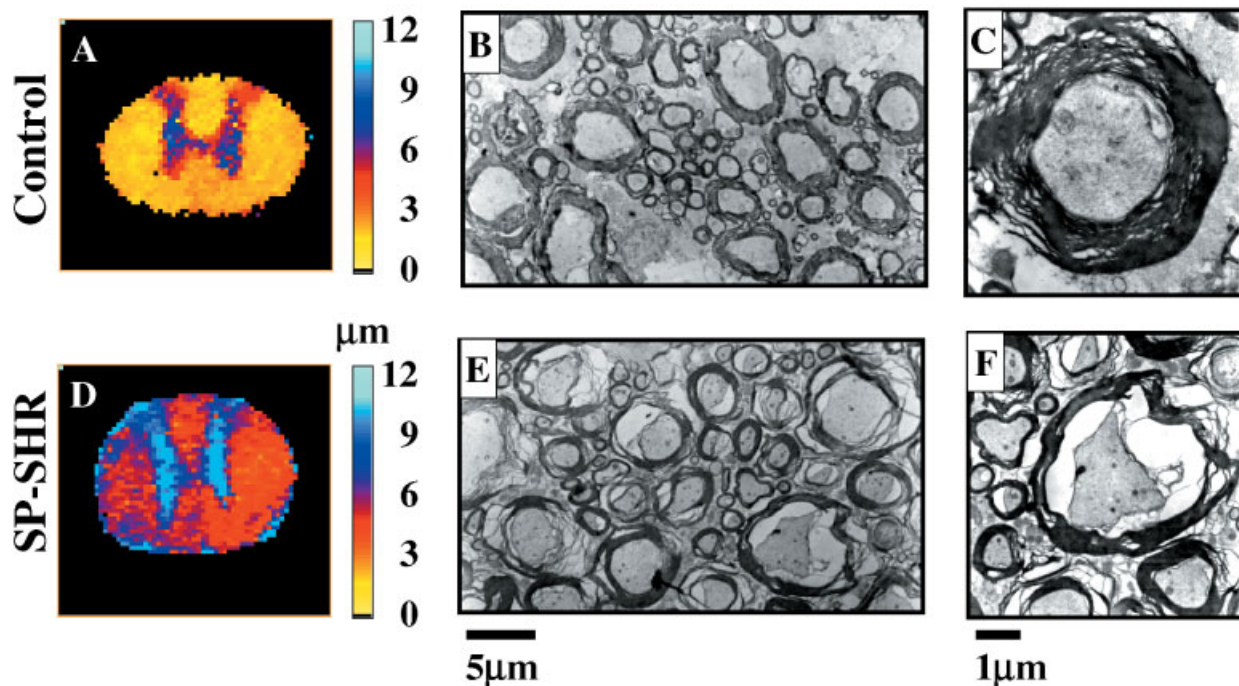
Indeed, the SP-SHR population developed motor impairment under conditions of a high-salt diet.[69] It was suspected that these impairments originated from small multiple ischemic lesions in their brains that are also projected into their spinal cords. In order to evaluate the diagnostic capacity of the high *b*-value **q**-space DWI approach we computed **q**-space MR images of spinal cords of a group of SP-SHRs and a group of age-matched control rats. In this study, diffusion anisotropy at low *b*-values ($b_{max} = 2500$ s mm^{-2}) and high *b*-value **q**-space MR images were acquired for the two groups *in vitro*. The diffusion data collected from ROIs that encompass the entire white matter of the spinal cords of these two groups are given in Fig. 16. Figure 16(A) shows the natural logarithm of the normalized signal intensity for the low *b*-value range ($b_{max} = 2500$ s mm^{-2}) while Fig. 16(B) shows the normalized signal-decay curves, on a logarithmic

Figure 16. Diffusion data for SP-SHR spinal cords ($n = 5$) and control Wistar rats spinal cords ($n = 4$). (A) Diffusion anisotropy measurements at low b-values up 2.5×10^3 s mm^{-2}. The diffusion gradients were applied along the z direction (parallel to the spinal cord long axis, represented by the // symbol) and along the x direction (perpendicular to the spinal cord long axis, represented by the $\perp$ symbol). (B) Signal decay as a function of b when diffusion was measured perpendicular to the spinal cord long axis for the high b-value range (up to 1×10^5 s mm^{-2}). The data were acquired with the same system and with the parameters given in caption of Figure 14.[69]
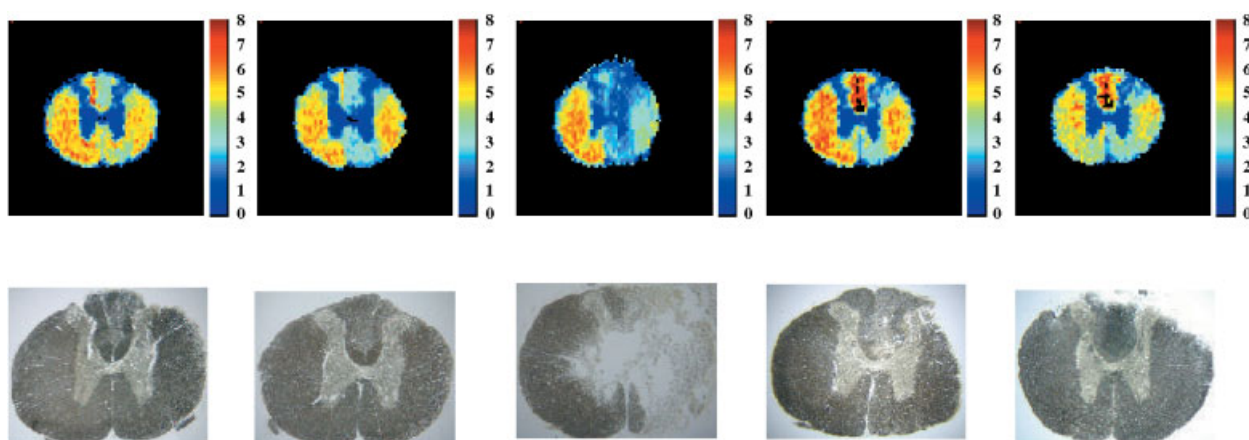
scale, of the control and SP-SHR groups for the entire range of b-values (up to b_{max} of 1×10^5 s mm^{-2}). This figure shows that the differences between the control and SP-SHR groups are much more pronounced at the high b-value range. Figure 16(A) demonstrates also that the

diffusion anisotropy index computed from the low b-values range (up to 2.5×10^3 s mm^{-2}) shows no significant differences between the SP-SHR and the control groups. However, the population fraction of the slow-diffusing component at high b-values was significantly smaller in

Figure 17. q-Space displacement image of a spinal cord of a control rat along with (B) EM image ($\times 1500$) and (C) a magnification of a single axon ($\times 5000$) of the same rat spinal cord shown in (A) showing the nearly intact myelin around the axon. (D) **q**-Space displacement image of a spinal cord of a SPSHR rat along with (E) EM image ($\times 1500$) and (F) a magnification of a single axon ($\times 5000$) of the same rat spinal cord shown in (D) showing the progressive demyelination and reduction in number of myelin wraps around the axon. For experimental details see Fig. 14.[69]

Figure 18. q-Space probability MR images (upper panel) and osmium staining (lower panel) of a rat spinal cord 6 weeks after 60 s hemi-crush trauma. The trauma site is the central slice (slice 3 out of the five slices shown).[72,73]

the SP-SHR group than in the control group (51 ± 2 *vs* $67 \pm 2\%$ respectively).[69] The mean displacement increased from a value of $2.2 \pm 0.3\,\mu m$ to a value of $3.8 \pm 0.7\,\mu m$ ($p < 0.03$), while the probability for the zero displacement decreased from 10.6 ± 1.4 (a.u.) to a value of 6.4 ± 0.9 (a.u.; $p < 0.03$).[69] These changes in the extracted **q**-space parameters, namely the increase in the mean displacement and the decrease in the probability for zero displacement, are in line with what is expected from axonal loss and demyelination. Interestingly, it was found that the anisotropy index at the low *b*-value range showed only a small reduction from a value of 0.84 ± 0.10 to 0.76 ± 0.11. This change was statistically non-significant. These results suggest the higher sensitivity toward this pathology of the high *b*-value **q**-space DWI, compared with the conventional diffusion anisotropy index computed from low *b*-value DWI. Figure 17 shows **q**-space displacement MR images of a control and SP-SHR spinal cords, along with electron microscopy (EM) of these spinal cords at two different magnifications. As expected for the SP-SHR spinal cord, where the mean displacement extracted from the **q**-space diffusion data is larger, a clear demyelination and neuronal degeneration is observed in the EM. The EM images show reduction in the thickness of the myelin in the SP-SHR spinal cords and the formation of large vacuoles between the axon and the disrupted myelin. These vacuoles may explain the increase in the average displacement in those spinal cords.
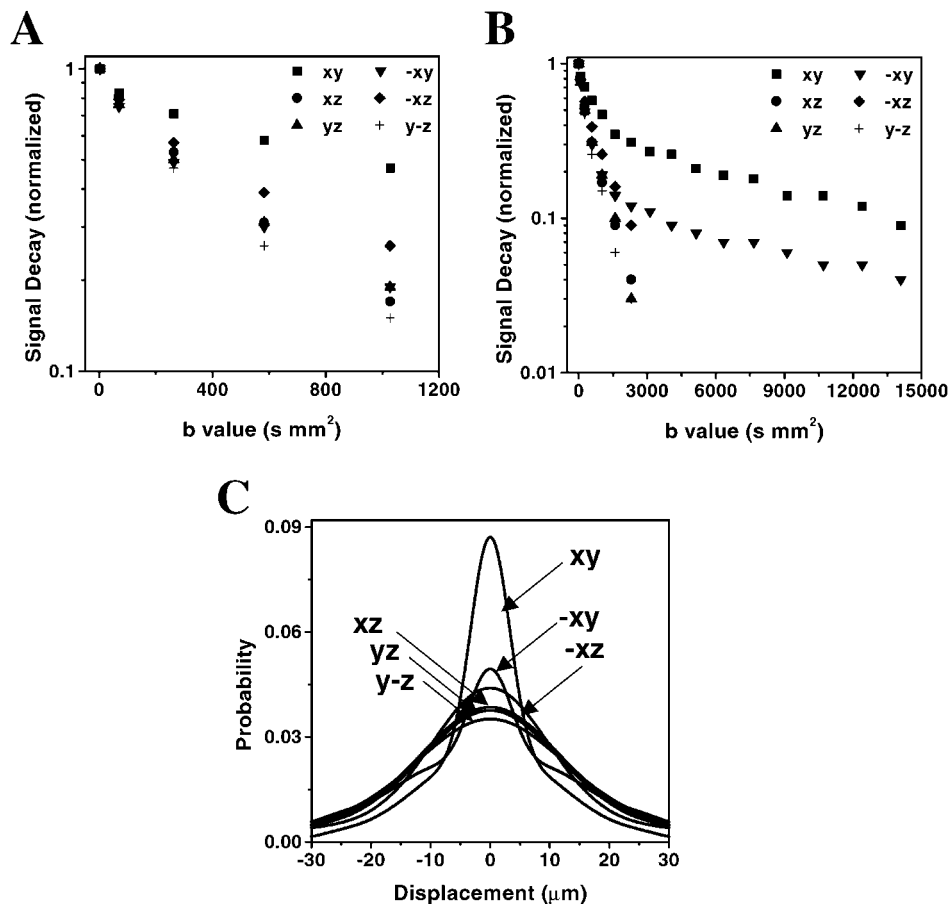
High *b*-value q-space DWI of spinal cord trauma[72,73]

High *b*-value **q**-space diffusion MRI was used also to study spinal cord trauma.[72,73] It is well known that spinal cord injury has devastating consequences and is therefore studied extensively.[74] These studies, which are directed towards finding ways to reverse or reduce the functional

loss associated with spinal cord injury, rely heavily on experimental models of spinal cord trauma and on methods for evaluating the pathophysiological state of the spinal cord. However, it was recently commented that one of the main problems in evaluating new spinal cord therapy is the relative difficulty in assessing the pathophysiological state of the spine.[75] Diffusion in general, and diffusion anisotropy in particular, was identified as a useful means of studying the spinal cord in the early days of DWI.[23] In recent years, there have been significantly more DWI studies of spinal cord morphology and pathology.[76–79] Here again, in most of the spinal cord diffusion studies, the data was analyzed using a mono-exponential decay, i.e. Stejskal–Tanner equation [eqn. (1)], and in a few the bi-exponential function shown in eqn. (2) (where $n = 2$) was used.[40] We therefore thought that spinal cord trauma, which may cause axon degeneration, might be more visible when using high *b*-value **q**-space DWI, especially for areas distant from the trauma site. Here high *b*-value **q**-space DWI was measured perpendicular to the long axis of the fibers of the spinal cord as seen in the upper panel of Fig. 18.[72,73]

Indeed high *b*-value **q**-space DWI was found to be sensitive to the hemi-crush model of the spinal cord and provided evidence for damage in areas remote from the trauma site even 6 weeks post-trauma for the 60 s hemi-crush as seen in Fig. 18. This Figure also demonstrates that at the trauma site and in remote areas where demyelination occurred there was a reduction in the probability for zero displacement. This decrease in the probability for zero displacement was accompanied by an increase in the mean displacement as expected for a demyelination process. As it was suggested that the apparent slow restricted diffusing component originates mainly from intra-axonal water,[64,66] for which the myelin serve as a barrier, the computed **q**-space images were compared with osmium staining for myelin. Indeed, in

A

B

C

Figure 19. The normalized water signal intensity as a function of b in the six different directions for b-values of up to (A) 1000, and (B) 14000 s mm^{-2}, respectively, for one pixel in the corpus callosum of a control subject. The displacement distribution profiles obtained by FT of the decay curves shown in (B). This data was obtained on a 1.5 T GE Signa horizon echo speed LX MRI scanner (GE, Milwaukee, WI, USA) using a spin echo diffusion EPI sequence with the following parameters: $TR/TE = 1500/167$ ms, $\Delta/\delta = 71/65$ ms and number of averages = 8.[58,89]

these experiments a good anatomical correlation between the **q**-space MR images and the osmium staining for myelin was observed, as seen in Fig. 18.[72,73]

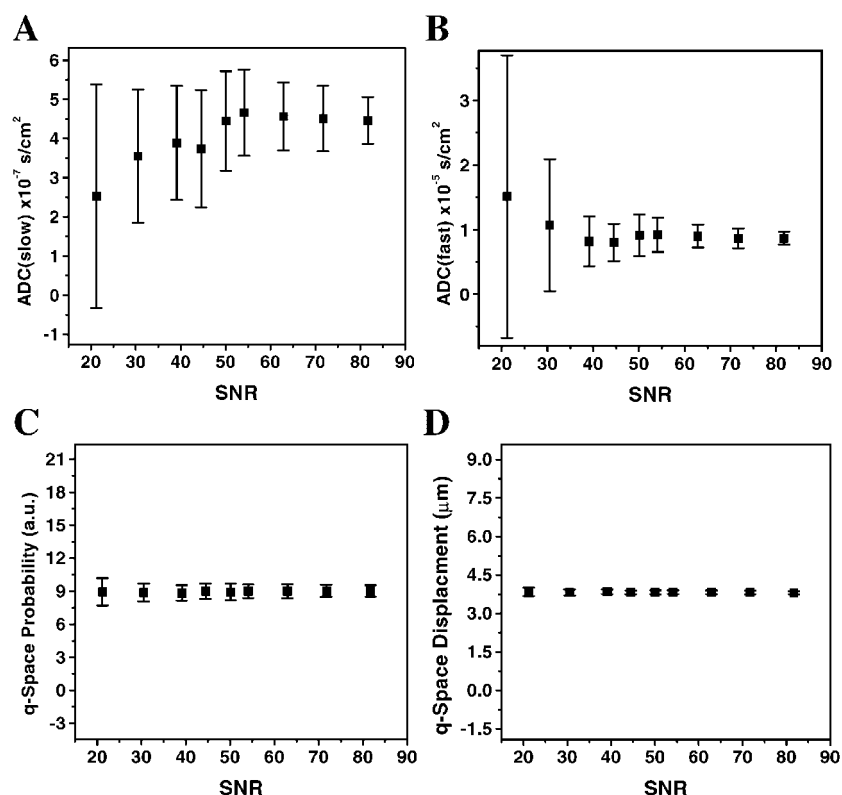## HIGH b-VALUE, q-SPACE DIFFUSION MRI OF THE HUMAN BRAIN: APPLICATION TO MULTIPLE SCLEROSIS

General considerations

The applications described so far have dealt with **q**-space DWI of spinal cords *in vitro*, acquired with the aid of a relatively strong pulse-gradient system. However, the full diagnostic capacity of the apparent slow-diffusing component should be evaluated and tested *in vivo* in human subjects. As it was found that the slow-diffusing component originates mainly from intra-axonal water, we thought to study first MS patients using high b-value **q**-space DWI, since this pathology is characterized by

demyelination.[80] However, two additional problems need to be overcome in order to apply the **q**-space DWI approach to the human brain.

Firstly, diffusion should be measured perpendicular to the long axis of the fibers, to get information on the average size of the compartment in which the diffusion takes place and maximize the effect of restriction. This is relatively easy to perform with excised spinal cord, where the main orientation of the fibers is known *a priori*. To overcome the problem of the different orientations of the fibers in brain tissue, the **q**-space analysis should be coupled with a tensor approach similar to that in DTI.[25,26] Here, one has to compute the **q**-space MR images by taking the minimal displacement and the maximal probability for zero displacement eigenvalues in each pixel, because these parameters represent diffusion perpendicular to the long axis of the fibers.

Secondly, **q**-space analysis of diffusion data requires powerful gradients of a kind not available on a clinical scanner. As mentioned before, the **q**-space analysis of

Figure 20. The effect of the SNR on the (A) ADC_{slow}, (B) ADC_{fast} extracted from a bi-exponential fit and on the (C) **q**-space probability, and (D) the **q**-space displacement from the **q**-space analysis of human diffusion data. The data were acquired with the parameters outlined in Fig. 19 with different number of averages in each experiment. A voxel of 3×3 pixels at the corpus callosum was used for the analysis. The *y*-axis in each of the figures was scaled to be $\pm 150\%$ of the value at the smallest SNR for comparison of the standard deviation between all figures

MR diffusion data was derived using the SGP approximation,[41,42] which implies that δ should be much shorter than Δ and significantly smaller than $a^2/2D$, where a is the size of the compartment in which the diffusion occurs. Evidently, these conditions are violated when one tries to achieve high diffusion weighting on a clinical MRI scanner, in which the gradient systems are capable of producing pulse-gradients of only a few Gauss/cm^{-1}.
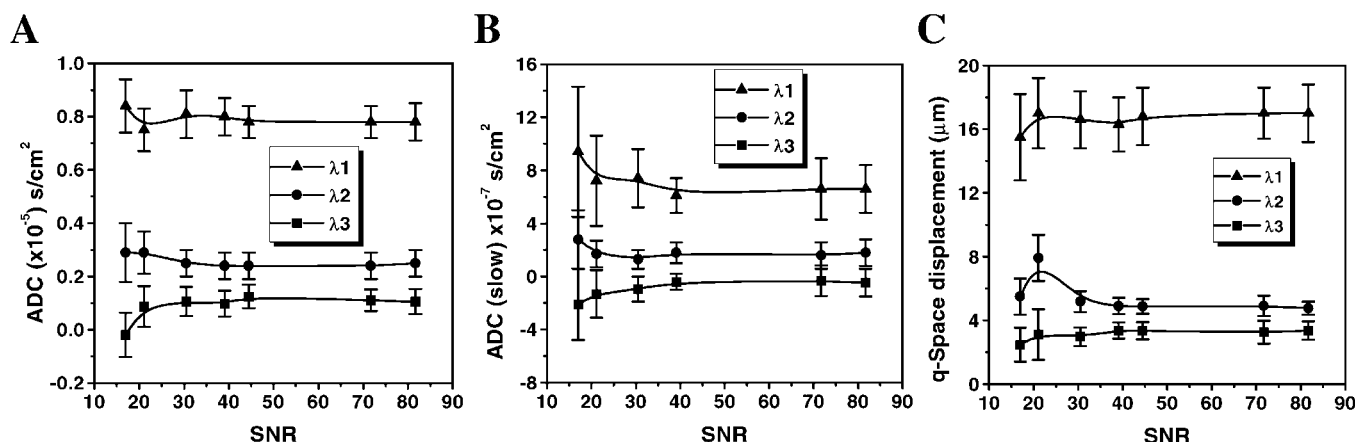
In addition, one has to obtain a suitable resolution and an adequate signal-to-noise ratio (SNR). Adequate SNR and noise are severe problems of DWI and DTI studies of human subjects, which become even more severe when high *b*-value DWI data are acquired in the clinical environment.

High *b*-value DWI of human subjects: q-space vs bi-exponential fit

Since the hardware available on a clinical scanner implies the use of experimental conditions that violate the conditions for which the **q**-space approach was derived, one may question the benefit, or even the legitimacy, of

using this approach under these experimental conditions. It seems much more straightforward to use the more familiar bi-exponential fit, which appears to be a more robust and reliable fitting procedure.

As the fiber orientation is not known *a priori* in the brain, any method of analysis selected will have to be coupled to a tensor analysis in order to determine the principal diffusivities in each voxel. Figure 19(A–B) shows the log of the normalized water signal intensity as a function of b, for b-values of up to 1000 and 14 000 s mm^{-2}, respectively. The data presented in Fig. 19 were taken from an ROI in the corpus callosum of a control subject in six non-collinear directions. From the bi-exponential fit of the high *b*-value data shown in Fig. 19(B), one can extract ADC_{fast} and ADC_{slow}. Figure 19C shows the six respective displacement distribution profiles, obtained by FT, of the decay curves shown in Fig. 19(B). From the data in Fig. 19 it is clear that the principal diffusivities are not the same for the different analyses. For example, using a bi-exponential fit, a very similar ADC_{slow} is found for the *xy* and $-xy$ directions, while using the **q**-space analysis there is a clear preference of the *xy* direction as a main contributor to

Figure 21. The effect of the SNR on the principal eigenvalues λ_1, λ_2, λ_3 for the (A) ADC extracted from conventional DTI, (B) ADC_{slow} extracted from a bi-exponential fit and the (C) **q**-space displacement from the **q**-space analysis of human diffusion data. The data were acquired with the parameters outlined in Fig.19, with different number of averages in each experiment. A voxel of 3×3 pixels at the corpus callosum was used for the analysis

the smallest eigenvalue that should represent the diffusion perpendicular to the principal axis of the fibers.
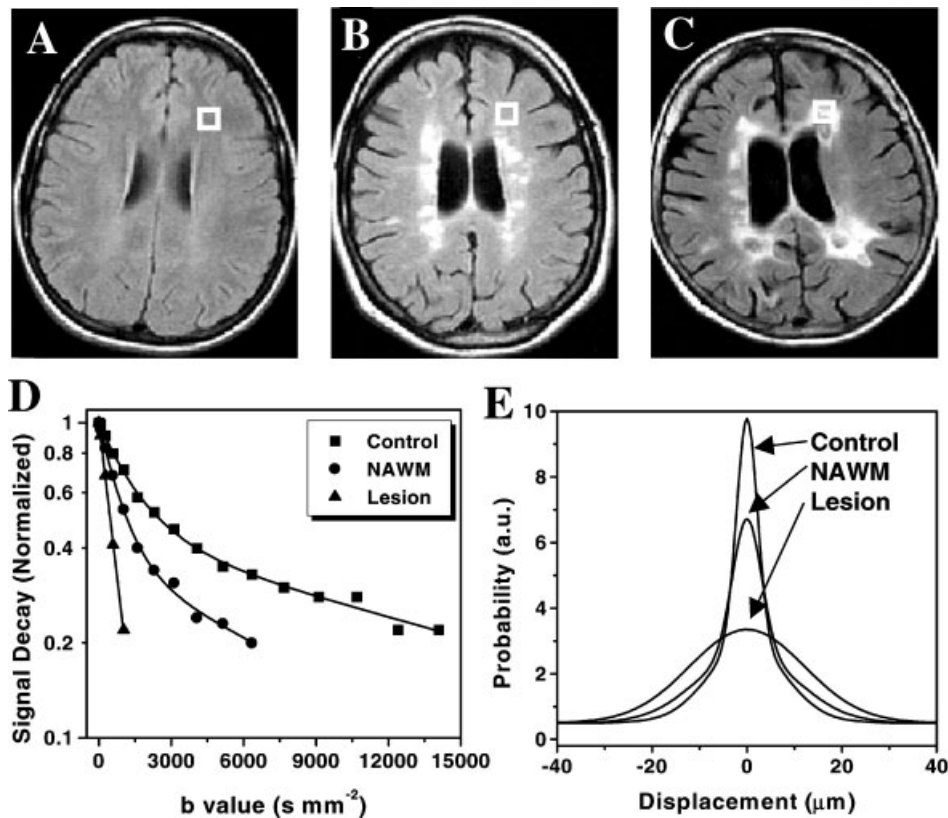
The data in Fig. 19(B) also demonstrate the difficulty of performing the DTI analysis on the slow diffusing component without incorporating some external subjective constraints. For many voxels, the decay curves are bi-exponential only in some of the directions sampled. In other directions a clear mono-exponential signal decay is observed, requiring a decision-making procedure that will determine whether a mono- or a bi-exponential function should be used to fit the data in each direction for a specific voxel. In fact, it was found that, in the bi-exponential fit, convergence occurred, in the same data set, about 40 times slower than in the **q**-space analysis on the same data set.

An additional factor that may affect the selection of the type of analysis one uses is the sensitivity of the extracted parameters to noise, as it is clear that high *b*-value DWI data suffer from intrinsically relative low SNR. To evaluate experimentally the effect of noise and SNR on the robustness of the parameters extracted from the different analysis, the same data set was analyzed at different SNR. Figure 20 shows the effect of SNR on the extracted ADC_{slow} and ADC_{fast} parameters obtained from the bi-exponential fit and the displacement and probability for zero displacement obtained from the **q**-space analysis of the same data set. These data were all taken from an ROI in the corpus callosum of a human subject after performing a diffusion tensor analysis on the bi-exponential fit functions and on the displacement distribution profiles. The data in Fig. 20 shows that the influence of the noise on the parameters extracted from the bi-exponential fit is much stronger, even at relatively high SNR. This effect becomes even more pronounced as the SNR becomes smaller. All *y*-axis values in all sub-figs in Fig. 20 are scaled to be $\pm150\%$ of their initial values. This scaling was applied in order to allow comparison of the standard deviation values that reach

$\pm150\%$ for the ADC_{fast} parameter at the lowest SNR. The graphs in Fig. 20 show that the standard deviations (SDs) of the parameters extracted from bi-exponential fit are much larger than the SDs of the parameters extracted from the **q**-space analysis. In addition, we observed that the **q**-space parameters hardly changes when SNR decreases, while significant changes are observed for the parameters extracted from the bi-exponential fit (ADC_{fast} and ADC_{slow}).

The effect of noise on low *b*-value DTI analysis has been addressed previously.[81] It was shown, theoretically, that the smallest eigenvalue (which should represent the diffusion perpendicular to white matter fibers), becomes negative for SNR in the order of 20 or less.[81] Figure 21(A) shows that such a trend was indeed observed experimentally for the smallest eigenvalue (λ_3) extracted from conventional DTI. When this analysis was repeated for the bi-exponential fit of the high *b*-value DWI data, for the ADC_{slow}, it was found that λ_3 is negative even for much higher SNR [Fig. 21(B)]. This phenomenon was not found for the parameters extracted from the **q**-space analysis of the same experimental data, as shown in Fig. 21(C) for the mean displacement parameter. In fact, this analysis demonstrates that, out of the five parameters studied (ADC at low *b*-values, ADC_{slow}, ADC_{fast}, **q**-space displacement and **q**-space probability), ADC_{slow} obtained from the bi-exponential fit is the most sensitive parameter to noise. Indeed, in two very recent reports of the diffusion-tensor-based images of the slow diffusing component, the images were acquired with relatively large number of averages in order to increase the SNR.[82,83]

The SGP and long diffusion time conditions are essential for extracting true structural parameters. As described above, the effect of the pulse gradient length was tested experimentally (see Fig. 7), on excised sciatic nerve. It was found that, when the pulse length is increased by a factor of 16, the measured displacement

Figure 22. FLAIR images of (A) control subject, (B) and (C) MS patients. Specific regions of interest are superimposed on each of the images at the frontal-temporal white matter that represent in (A) control area, in (B) NAWM area and in (C) MS lesion area. (D) The signal decay as a function of *b*-values for the regions of interest shown on the FLAIR images. (E) The respective **q**-space profiles of the data are shown in (D) after data extrapolation (reproduced by permission of Wiley-Liss, Inc. from Assaf *et al.*[58,89])
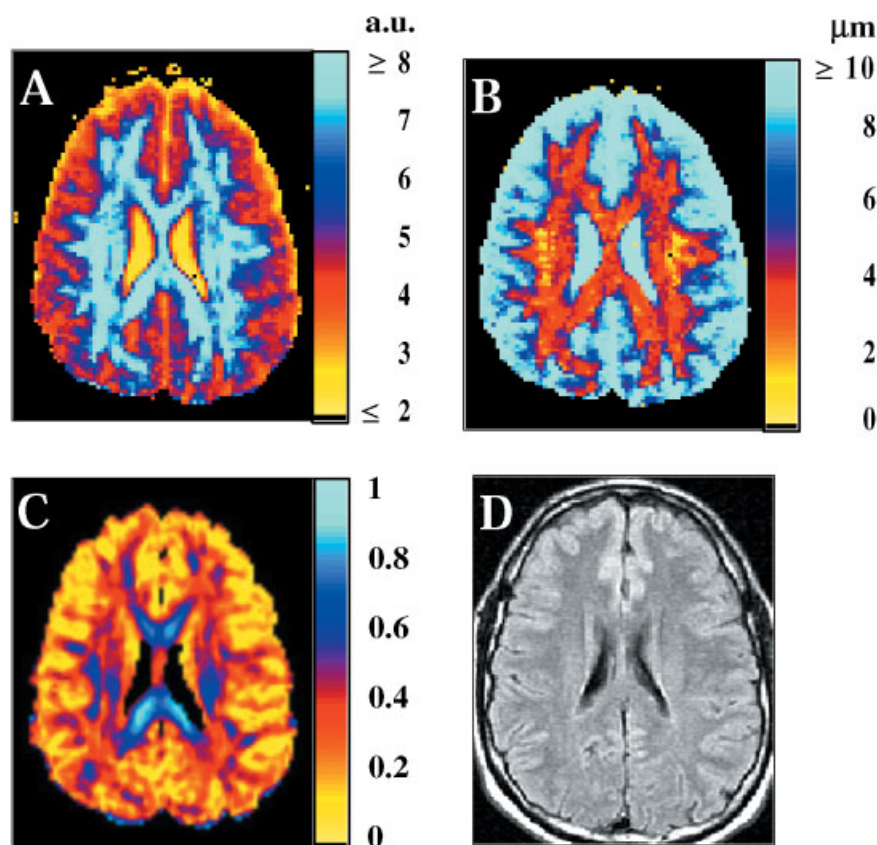
from the **q**-space profile decreases only by a factor of 2. In the brain, this effect might be even smaller, because exchange is faster than in nerve and contributes much more to the signal decay than restricted diffusion. The fact that by using long gradient pulses we get a narrowing of the displacement profile of the restricted component means that these experimental parameters slightly over-emphasize the relative population that exhibits restricted diffusion. However, it should be noted that the deviations in the absolute values of the **q**-space extracted parameters do not degrade our ability to use these parameters as a marker for the pathophysiological state of white matter in the same sense that the obtained ADC enabled us to diagnose ischemic tissues. It is the relative values of these parameters in control and diseased tissues that are used for diagnosing abnormal pathology.

High *b*-value q-space analyzed diffusion MRI of controls and MS brains[58,59]

MRI is a major imaging technique that supports the clinical diagnosis of multiple sclerosis (MS).[84,85] T_2-weighted MRI and fluid attenuated inversion recovery (FLAIR) are the conventional MR techniques that identify MS lesions and measure the disease load. Nevertheless, it was found that some areas that appear to be normal on conventional MR images have abnormal metabolite distribution as detected by MRS.[85,86] These areas were categorized as the normal appearing white matter (NAWM). DTI and magnetization transfer (MT) imaging have also been used recently to characterize the NAWM in MS patients.[21,28–30,84,85,87,88] Since the documented MT and DTI changes in the NAWM of MS are relatively small and MRS suffers from low spatial and temporal resolution, new imaging techniques with higher sensitivity for the disease load, particularly in the NAWM, are needed. Owing to the high sensitivity of high *b*-value **q**-space DWI towards restricted water diffusion, and the result obtained from animal models that showed that demyelination is detected with great sensitivity by the **q**-space approach, this method was tested and used to study MS in human brains.

In the white matter of control brains the water signal decay was found to be multi-exponential at high *b*-values, at least in some gradient directions. The deviation from
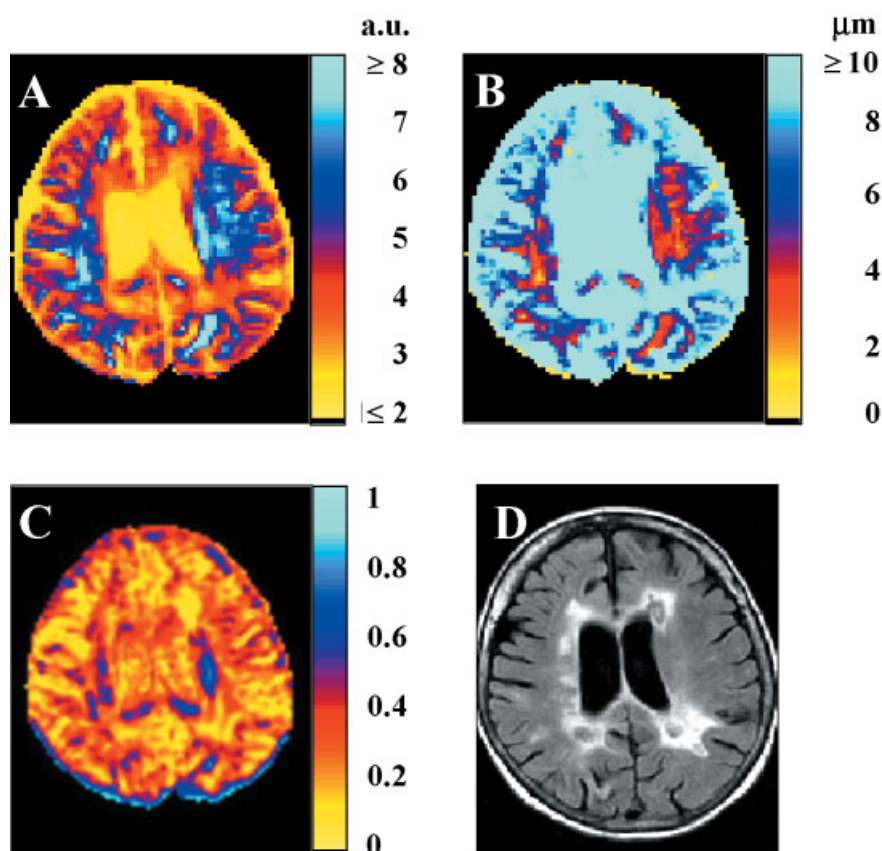
Figure 23. MRI data set of a control subject. (A) A **q**-space probability image, (B) a **q**-space displacement image, (C) a FA image, and (D) a FLAIR image. This data was obtained on a 1.5 T GE Signa horizon echo speed LX MRI scanner (GE, Milwaukee, WI, USA). The **q**-space diffusion data was obtained using a spin echo diffusion EPI sequence with the following parameters: *TR/TE* = 1500/167 ms, Δ/δ = 71/65 ms and number of averages = 8.[58,89]

mono-exponential decay was observed at *b*-values higher than $\sim$3000 s mm^{-2} as reported previously.[37–39] Figure 22(A–C) shows FLAIR images of a control subject and two MS patients, respectively, on which specific ROIs at the tempo-frontal white matter are depicted. The ROIs shown in Figs. 22(A–C) represents normal white matter, NAWM and MS lesion ROIs, respectively. The diffusion signal decays and the respective **q**-space displacement profiles (after data extrapolation) from these ROIs are depicted in Fig. 22(D, E), respectively. The signal decays shown are those obtained when the diffusion gradient direction was perpendicular to the computed general fibers' orientation in these specific ROIs. The slow diffusing component, which is very prominent in the control ROI, is less apparent in the NAWM ROI, and is completely absent in the MS lesion ROI [Fig. 22(D)].[89] Indeed, the **q**-space displacement distribution profiles of these three ROIs were found to be different. There is a gradual decrease in the amplitude and broadening of the displacement distribution profiles when moving from the control ROI to the NAWM ROI and to the MS lesion ROI.

Figure 23(A, B) shows representative probability and displacement **q**-space analyzed MR images of a normal subject. In those images the contrasts are the probability for zero displacement and the apparent mean displacement given in arbitrary units and in μm, respectively. From the **q**-space analysis it is clear that, using the experimental parameters used in this study,[89] the apparent displacement in white matter is about 2–4 μm. Under these experimental conditions the apparent displacements are 7–9 μm for gray matter, and higher than 10 μm for the CSF [Fig. 23(B)]. The calculated probability for zero displacement, however, is significantly higher in white matter than in gray matter [Fig. 23(A)]. For comparison, Fig. 23(C) and (D) show the fractional anisotropy (FA) image obtained from conventional DTI (using the same color-map as in the **q**-space images) and the FLAIR image on the same brain, respectively.

Figure 24 shows the same MRI data set for a representative case of a severe MS patient having many lesions. These periventricular lesions (MS plaques) appear as hyperintense areas in the FLAIR image [Fig.

Figure 24. MRI data set of a severe MS patient. (A) A **q**-space probability image, (B) a **q**-space displacement image, (C) an FA image, and (D) a FLAIR image. For experimental details see Fig. 23.[58,89]
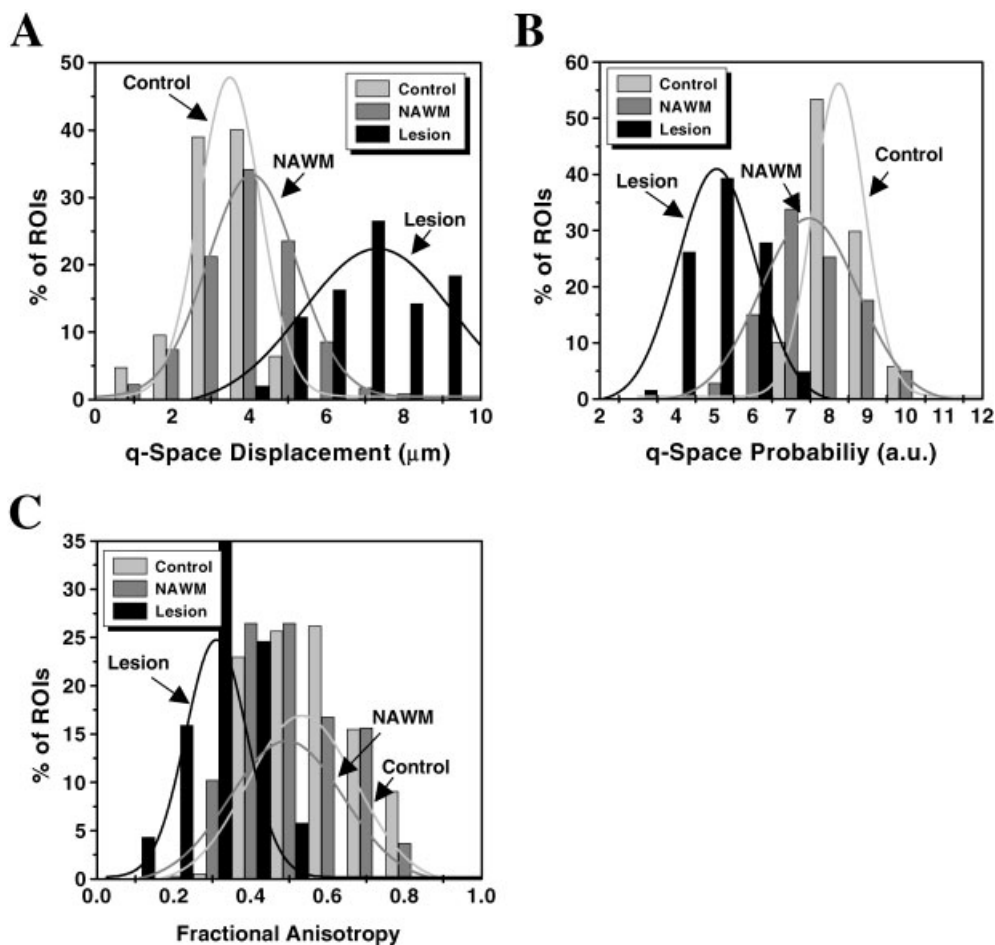
24(D)]. In the **q**-space MR images [Fig. 24(A, B)], however, these lesions are characterized by lower probability and larger displacement values, compared with the values obtained for similar anatomical areas in brains of control subjects.

Figure 25 presents the histograms of the different indices, calculated from the ROI analysis of the entire population studied, for the three different groups of ROIs (control, NAWM and MS lesion ROIs). These ROIs were classified using the FLAIR images as either lesion or NAWM. The control brains were used to obtain the control values of these respective ROIs. In this analysis, 35 ROIs in each brain of the six control subjects and 13 MS patients were studied. Figure 25(A) and (B) show the histograms of the ROI analysis for the **q**-space displacement and probability values, respectively. The differences between the histograms of the **q**-space indices of the control and the MS plaque are highly significant. For the NAWM ROIs of MS patients, the histogram of the **q**-space indices appears between the two histograms, suggesting that some of these ROIs have abnormal probability and displacement values, while other ROIs in this group have control values. Figure 25(C) shows the ROI histogram for the FA values obtained from

conventional DTI analysis with $b = 1000 \text{ s mm}^{-2}$ derived from the same data used to obtain the **q**-space analysis. This figure shows that the FA ROI histograms are different for control ROIs and MS lesion ROIs. However, the histograms of the FA extracted from conventional DTI show small differences between control and the NAWM ROIs. The numerical values of the **q**-space and the DTI indices of this analysis appear in Table 1.

High *b*-value q-space DWI as a potential diagnostic tool for MS

At high *b*-value DWI, an apparent slow-diffusing component that exhibits restricted diffusion is observed. As it was found that intra-axonal water contributes significantly to this component, one can hypothesize that it would be more sensitive to the physiological state of white matter. Indeed, it was found that the indices extracted from the **q**-space analysis of high *b*-value DWI data provides MR images that seem to characterize better the disease load in MS, compared with other conventional MRI methods. The changes in the mean displacement and the probabilities for zero displacement

Figure 25. ROI histograms for (A) the **q**-space displacement index, (B) **q**-space probability index and (C) the FA for the control, NAWM and MS lesion ROIs. The numerical data of this ROI analysis is summarized in Table 1.[58,89]

extracted from the **q**-space analysis of the slow diffusing component are even more prominent and pronounced than the changes in the FA obtained from conventional DTI, as suggested by the histograms shown in Figure 25 and the numerical values given in Table 1.

The **q**-space-analyzed MR images suggest that the abnormalities in MS brain are not concentrated only in the hyperintense areas seen on the T_2 images, but are of a more global nature that is consistent with the known occurrence of diffuse axonal loss in advanced MS. The

main contribution of high *b*-value **q**-space diffusion MR images seems to be in the evaluation of the diffused pathology in areas classified as NAWM in the FLAIR MR images. Furthermore, areas that appeared significantly abnormal in the **q**-space analyzed MR images proved to be abnormal in DTI, but with lower statistical significance. This is true both for the MS plaques and, more importantly, in the so-called NAWM. This might suggest that high *b*-value **q**-space MR images could increase our ability to identify areas of abnormal NAWM

Table 1. ROI analysis of q-space and DTI data for MS and control brains[a,b,89]

ROI	Probability	Displacement (µm)	FA
Control	8.3 ± 0.7	3.3 ± 0.8	0.56 ± 0.12
NAWM	7.5 ± 1.1 ($p < 1 \times 10^{-9}$)	4.0 ± 1.2 ($p < 1 \times 10^{-9}$)	0.51 ± 0.13 ($p < 1 \times 10^{-6}$)
MS lesion	5.0 ± 0.9 ($p < 1 \times 10^{-9}$)	8.1 ± 2.4 ($p < 1 \times 10^{-9}$)	0.32 ± 0.08 ($p < 1 \times 10^{-6}$)

[a] Values are averages $\pm$ SD.
[b] *p*-Values are the results of an independent *t*-test compared with the control values in the first row.

in a single subject. However apparent, a clear statement about the diagnostic capacity of the slow-diffusing component, compared with conventional DTI with respect to the NAWM, should await more extensive comparisons between the high *b*-value **q**-space DWI and conventional DTI indices as compared to, for example, the NAA distribution as obtained from MRS.

CONCLUSIONS AND FUTURE PROSPECTS OF HIGH *b*-VALUE q-SPACE DWI

New and more specific MR images may increase the diagnostic capability of MRI. Diffusion can be regarded as a filtering method and it was found to increase our ability to detect acute cerebral ischemia.[5–13] The fact that an additional diffusing component is apparent in CNS tissue at high diffusion weighting (high *b*-values) raises a question regarding the diagnostic capacity of this component. As we found that this component originates mainly from intra-axonal water,[65,66] we thought that the **q**-space approach would be sensitive to the physiological and pathological states of white matter.

When the signal decay is not mono-exponential there are different approaches to analyzing the data. The analysis of high *b*-value DWI data by the **q**-space approach may be beneficial for the following reasons. First, this approach provides a means of obtaining non-invasive structural information about the sample just by performing a FT on the raw data. Indeed, in *in vitro* systems like in spinal cord, MR images can be obtained in which the mean displacement provides structural information on a microns scale.[65,66,68] The mean displacement extracted from the **q**-space MRI data correlated with EM data in these *in vitro* systems. This means that this approach can provide, in such systems, information that is comparable to low resolution EM. An additional important feature of the **q**-space approach is that it allows detection of restricted diffusion in a relatively straightforward manner, just by following the changes in the displacement probability profiles as a function of the diffusion time.[90] It was also found that **q**-space diffusion MRS and MRI are extremely sensitive to the pathophysiological state of the white matter. So far, this approach was used to study spinal cord maturation,[68] experimental allergic neuritis (EAN)[57,67] spinal cord trauma[72,73] and vascular dementia *in vitro*,[69] and MS in human subjects.[58,89] In all these studies, high *b*-value **q**-space diffusion MRS and MRI were found to be very sensitive to the pathophysiological state of white matter. In the *in vitro* systems, when one uses strong gradient systems, the mean displacement obtained from the **q**-space analysis reports on the compartment size in which the diffusion takes place with relatively high accuracy. It should be noted, however, that when using clinical scanners the **q**-space analysis does not provide accurate compartment sizes. As pointed out, the violation of the SGP

approximation results in mean displacements that are smaller than the real size of the compartment in which the diffusion occur. Nevertheless, the **q**-space approach seems to be suitable for exploring the potential diagnostic capacity embedded in the apparent slow-diffusing component observed at high *b*-value at long diffusion time. One of the main limitations of high *b*-value **q**-space DWI, however, is the relatively long acquisition time needed to obtain such data sets. This is because high *b*-value DWI data suffers from low SNR and because, in order to perform the **q**-space analysis, one has to acquire a relatively large number of DW images with different **q**-values that should be collected for at least six directions, as in DTI. All these requirements result in a relatively long acquisition time. For example, in the **q**-space MS study the data set required for the **q**-space analysis was acquired in 24 min using a diffusion-weighted spin-echo EPI sequence. However, since high *b*-value DWI reduces the contribution of water from different compartments leaving mostly intra-axonal water, it seems plausible to speculate that high *b*-value **q**-space DWI might increase our ability to study maturation and degeneration of the CNS, as well as white-matter associated disorders in general.

Two important and promising directions that were not dealt with in the current review are the applications of **q**-space MRI to distinguish between diffusion and coherent slow flow[91–94] and the Wedeen's diffusion spectrum imaging approach for fiber tracking.[95,96] Recent works by Van As has demonstrated the potential of this approach[93,94] for such a separation, work that originated from Callaghan early papers on **q**-space diffusion MRI.[91,92] Diffusion spectrum imaging suggested by Wedeen[95,96] seems to be a promising approach to resolve intravoxels orientational heterogeneity and await future development.

Water is found in all compartments in the CNS and diffusion can be regarded as a filtering method. In high *b*-value DWI, few water components can be resolved. If the different components represent different entities or originate mainly from different water pools it seems logical to assume that proper analysis of such data set will increase the MRI specificity and diagnostic capacity. Among the different approaches available for analyzing such diffusion data set it seems that the **q**-space is an attractive approach and that efforts should be made to evaluate the utility of the structural and pathophysiological information that can be extracted from this approach.

REFERENCES

1. Stark DD, Bradley WG. Magnetic Resonance Imaging, 3rd edn. Mosby: St Louis, Mo, 1999.
2. Norris DG. The effects of microscopic tissue parameters on the diffusion weighted magnetic resonance imaging experiment. *NMR Biomed.* 2001; **14**: 77–93.
3. Le Bihan D, Berton E, Lallemand D, Grenier P, Cabanis E, Laval-Jeantet M. MR imaging of intravoxel incoherent motions: application to diffusion and perfusion in neurologic disorders. *Radiology* 1986; **161**: 401–407.
4. Le Bihan D, Breton E, Lallemand D, Aubin ML, Vignaud J, Laval-Jeantet M. Separation of diffusion and perfusion in intravoxel incoherent motion MR imaging. *Radiology* 1988; **168**: 497–505.
5. Moseley ME, Cohen Y, Mintorovitch J, Chileuitt L, Shimizu H, Kucharczyk J, Wendland MF, Weinstein PR. Early detection of regional cerebral ischemia in cats-comparison of diffusion-weighted and T2-weighted MRI and spectroscopy. *Magn. Reson. Med.* 1990; **14**: 330–346.
6. Minematsu K, Li L, Fisher M, Sotak CH, Davis MA, Fiandaca MS. Diffusion-weighted magnetic resonance imaging for rapid and quantitative detection of focal brain ischemia. *Neurology* 1992; **42**: 235–240.
7. Busza AL, Allen KL, King MD, van Bruggen N, Williams SR, Gadian DG. Diffusion weighted imaging studies of cerebral ischemia in gerbils—potential relevance to energy failure. *Stroke* 1992; **23**: 1602–1162.
8. Mintorovitch J, Moseley ME, Chileuitt L, Shimizu H, Cohen Y, Weinstein PR. Comparison of diffusion-weighted and T2-weighted MRI for the early detection of cerebral ischemia and reperfusion in rats. *Magn. Reson. Med.* 1991; **18**: 39–50.
9. van Bruggen N, Cullen BM, King MD, Doran M, Williams SR, Gadian DG, Cremer JE. T2-weighted and diffusion-weighted magnetic resonance imaging of a focal ischemic lesion in rat brain. *Stroke* 1992; **23**: 576–582.
10. Neumann-Haefelin T, Kastrup A, de Crespigny A, Yenary MA, Ringer T, Sun GH, Moseley ME. Serial MRI after transient focal cerebral ischemia in rats—dynamics of tissue injury, blood–brain barrier, and edema formation. *Stroke* 2000; **31**: 1965–1972.
11. Hossmann KA, Hoehn-Berlage M. Diffusion and perfusion MR imaging of cerebral ischemia. *Cerebrovas. Brain Metab.* 1995; **7**: 187–217.
12. Hoehn-Berlage M. Diffusion-weighted NMR imaging: application to experimental focal cerebral ischemia. *NMR Biomed.* 1995; **8**: 345–358.
13. Schaefer PW, Grant PE, Gonzalez RG. Diffusion-weighted MR imaging of the brain. *Radiology* 2000; **217**: 331–345.
14. Decanniere C, Eleff S, Davis D, Zijl PCM van. Correlation of rapid changes in the average water diffusion constant and the concentrations of lactate and ATP breakdown products during global ischemia in cat brain. *Magn. Reson. Med.* 1995; **34**: 343–352.
15. Nicolay K, Braun KPJ, Graaf RA de, Dijkhuizen RM, Kruiskamp MJ. Diffusion NMR spectroscopy. *NMR Biomed.* 2001; **14**: 94–111.
16. Eis M, Els T, Hoehn-Berlage M. High-resolution quantitative relaxation and diffusion MRI of 3 different experimental brain tumors in rat. *Magn. Reson. Med.* 1995; **34**: 835–844.
17. Assaf Y, Holokovsky A, Berman E, Shapira Y, Shohami E, Cohen Y. Diffusion and perfusion magnetic resonance imaging following closed head injury in rats. *J. Neurotrauma* 1999; **16**: 1165–1176.
18. Alsop DC, Murai H, Detre JA, McIntosh TK, Smith DH. Detection of acute pathologic changes following experimental traumatic brain injury using diffusion-weighted magnetic resonance imaging. *J. Neurotrauma* 1996; **13**: 515–521.
19. Ahrens ET, Laidlaw DH, Readhead C, Brosnan CF, Fraser SE, Jacobs RE. MR microscopy of transgenic mice that spontaneously acquire experimental allergic encephalomyelitis. *Magn. Reson. Med.* 1998; **40**: 119–132.
20. Takano K, Latour LL, Formato JE, Carano RAD, Helmer KG, Hasegawa Y, Sotak CH, Fisher M. The role of spreading depression in focal ischemia evaluated by diffusion mapping. *Ann. Neurol.* 1996; **39**: 308–318.
21. Cercigani M, Iannuci G, Rocca MA, Comi G, Horsfield MA, Filippi M. Pathologic damage in MS assessed by diffusion-weighted and magnetization transfer MRI. *Neurology* 2000; **54**: 1139–1144.
22. Ono J, Harada K, Takahashi M, Maeda M, Ikenaka K, Sakurai K, Sakai N, Kagawa T, Fritzzieroth B, Nagai T, Nihei A, Hashimoto S, Okada S. Differentiation between dysmyelination and demyelination using magnetic-resonance diffusional anisotropy. *Brain Res.* 1995; **671**: 141–148.
23. Moseley ME, Cohen Y, Kucharczyk J, Mintorovitch J, Asgari HS, Wendland MF, Tsuruda J, Norman D. Diffusion-weighted MR imaging of anisotropic water diffusion in cat central nervous system. *Radiology* 1990; **176**: 439–445.
24. Chenevert TL, Brunberg JA, Pipe JG. Anisotropic diffusion in human white matter—demonstration with MR techniques in-vivo. *Radiology* 1990; **177**: 401–405.
25. Basser PJ, Mattiello J, LeBihan D. MR diffusion tensor spectroscopy and imaging. *Biophys. J.* 1994; **66**: 259–267.
26. Basser PJ, Pierpaoli C. A simplified method to measure the diffusion tensor from seven MR images. *Magn. Reson. Med.* 1998; **39**: 928–934.
27. Basser PJ, Pajevic S, Pierpaoli C, Duda J, Aldroubi A. In vivo tractography using DT-MRI data. *Magn. Reson. Med.* 2000; **44**: 625–632.
28. Bammer R, Augustin M, Strasser-Fuchs S, Seifert T, Kapeller P, Stollberger R, Ebner F, Hartung HP, Fazekas F. Magnetic resonance diffusion tensor imaging for characterizing diffuse and focal white matter abnormalities in multiple sclerosis. *Magn. Reson. Med.* 2000; **44**: 583–91.
29. Werring DJ, Clark CA, Barker GJ, Thompson AJ, Miller DH. Diffusion tensor imaging of lesions and normal-appearing white matter in multiple sclerosis. *Neurology* 1999; **52**: 1626–1632.
30. Klingberg T, Hedehus M, Temple E, Salz T, Gabrieli J, Moseley M, Poldrack R. Microstructure of temporo-parietal white matter as a basis for reading ability: Evidence from diffusion tensor magnetic resonance imaging. *Neuron* 2000; **25**: 493–500.
31. Stejskal EO, Tanner JE. Spin diffusion measurements: spin echoes in the presence of a time-dependent field gradient. *J. Chem. Phys.* 1965; **42**: 288–292.
32. Niendorf T, Norris DG, Leibfritz D. Detection of apparent restricted diffusion in healthy rat brain at shot diffusion time. *Magn. Reson. Med.* 1994; **32**: 672–677.
33. Assaf Y, Cohen Y. Detection of different water populations in brain tissue using 2H single- and double-quantum-filtered diffusion NMR spectroscopy. *J. Magn. Reson. B* 1996; **112**: 151–159.
34. Niendorf T, Dijkhuizen RM, Norris DG, van Lookeren Campagne M, Nicolay K. Biexponential diffusion attenuation in various states of brain tissue: implications for diffusion-weighted imaging. *Magn. Reson. Med.* 1996; **36**: 847–857.
35. Stanisz GJ, Szafer A, Wright GA, Henkelman RM. An analytical model for restricted diffusion in bovine optic nerve. *Magn. Reson. Med.* 1997; **37**: 103–111.
36. Assaf Y, Cohen Y. Non-mono-exponential attenuation of water and N-acetyl aspartate signals due to diffusion in brain tissue. *J. Magn. Reson.* 1998; **131**: 69–85.
37. Mulkern RV, Gugbjartsson H, Westin CF, Zengingonul HP, Gartner W, Guttmann CRG, Robertson RL, Kyriakos W, Schwartz R, Holtzman D, Jolesz FA, Maier SE. Multi-component apparent diffusion coefficients in human brain. *NMR Biomed.* 1999; **12**: 51–62.
38. Mulkern RV, Zengingonul HP, Robertson RL, Bonger P, Zou KH,

Gudbjartsson H, Guttmann CRG, Holtzman D, Kyriakos W, Jolesz FA, Maier SE. Multi-component apparent diffusion coefficients in human brain: Relationship to spin-lattice relaxation. *Magn. Reson. Med.* 2000; **44**: 292–300.

39. Clark CA, Le-Bihan D. Water diffusion compartmentation and anisotropy at high *b*-values in the human brain. *Magn. Reson. Med.* 2000; **44**: 852–859.

40. Inglis BA, Bossart EL, Buckley DL, Wirth ED, Mareci TH. Visualization of neural tissue water compartments using biexponential diffusion tensor MRI. *Magn. Reson. Med.* 2001; **45**: 580–587.

41. Cory DG, Garroway AN. Measurement of translational displacement probabilities by NMR - An indicator of compartmentation. *Magn. Reson. Med.* 1990; **14**: 435–444.

42. Callaghan PT, Coy A, MacGowan D, Packer KJ, Zelaya FO. Diffraction-like effects in NMR diffusion studies of fluid in porous solids. *Nature* 1991; **351**: 467–469.

43. Andrasko J. Water diffusion permeability of human erythrocytes studied by a pulsed gradient NMR technique. *Biochem. Biophys. Acta* 1976; **428**: 304–311.

44. van Zijl PC, Moonen C, Faustino P, Pekar J, Kaplan O, Cohen J. Complete separation of intracellular and extracellular information in NMR spectra of perfused cells by diffusion-weighted spectroscopy. *Proc. Natl. Acad. Sci. USA* 1991; **88**: 3228–3232.

45. Callaghan PT, Codd SL, Seymour JD. Spatial coherence phenomena arising from translational spin motion in gradient spin echo experiments. *Concepts Magn. Reson.* 1999; **11**: 181–202.

46. Price WS. Pulsed-field gradient nuclear magnetic resonance as a tool for studying translational diffusion. 1. Basic theory. *Concepts Magn. Reson.* 1997; **9**: 299–336.

47. Callaghan P. Pulsed gradient spin echo NMR for planar, cylindrical and spherical pores under conditions of wall relaxation. *J. Magn. Reson. A* 1995; **113**: 53–59.

48. Coy A, Callaghan PT. Pulsed gradient spin echo nuclear magnetic resonance of molecules diffusing between partially reflecting rectangular barriers. *J. Chem. Phys.* 1994; **101**: 4599–4609.

49. Snaar JEM, Hills BP. Constant gradient stimulated echo studies of diffusion in porous materials at high spectrometer fields. *Magn. Reson. Imag.* 1997; **15**: 983–992.

50. Kuchel PW, Coy A, Stilbs P. NMR 'diffusion-diffraction' of water revealing alignment of erythrocytes in a magnetic field and their dimensions and membrane transport characteristics. *Magn. Reson. Med.* 1997; **37**: 637–643.

51. Kuchel PW, Durrant CJ. Permeability coefficients from NMR q-space data: Models with unevenly spaced semi-permeable parallel membranes. *J. Magn. Reson.* 1999; **139**: 258–272.

52. Torres AM, Michniewicz RJ, Chapman BE, Young GAR, Kuchel PW. Characterization of erythrocyte shapes and sizes by NMR diffusion-diffraction of water: Correlations with electron micrographs. *Magn. Reson. Imag.* 1998; **16**: 423–434.

53. Torres AM, Taurins AT, Regan DG, Chapman BE, Kuchel PW. Assignment of coherence features in NMR q-space plots to particular diffusion modes in erythrocyte suspensions. *J. Magn. Reson.* 1999; **138**: 135–143.

54. Peled S, Cory DG, Raymond SA, Kirschner DA, Jolesz FA. Water diffusion and compartmentation in frog sciatic nerve. *Magn. Reson. Med.* 1999; **42**: 911–918.

55. Johnson PT, Geller SF, Reese BE. Distribution, size and number of axons in the optic nerve pathway of ground squirrels. *Exp. Brain Res.* 1998; **118**: 93–104.

56. Mitra PP, Halperin B. Effect of finite gradient pulse width in pulsed-gradient diffusion measurements. *J. Magn. Reson. A* 1995; **113**: 94–101.

57. Assaf Y, Michal K, Shinar H, Chapman J, Korczyn AD, Navon G, Cohen Y. Early detection of the pathologies in experimental allergic neuritis using high-*b*-value q-space diffusion MRS. *Proc. Int. Soc. Magn. Reson. Med.* 2001; **9**: 509.

58. Assaf Y, Ben-Bashat D, Peled S, Chapman J, Segev Y, Hendler T, Korczyn AD, Graif M, Cohen Y. Evaluation of the physiological state of white matter by high *b*-value q-space analyzed diffusion weighted imaging: Applications to multiple sclerosis. *Proc. Int. Soc. Magn. Reson. Med.* 2001; **9**: 150.

59. King MD, Houseman J, Roussel SA, Bruggen N van, Williams SR, Gadian DG. q-Space imaging of the brain. *Magn. Reson. Med.* 1994; **32**: 707–713.

60. King MD, Houseman J, Gadian DG, Connelly A. Localized q-space imaging of the mouse brain. *Magn. Reson. Med.* 1997; **38**: 930–937.

61. Assaf Y, Cohen Y. Diffusion of water and metabolites in brain tissue as a function of the diffusion time. *Proc. Int. Soc. Magn. Reson. Med.* 1997; **5**: 1254.

62. Assaf Y, Cohen Y. Diffusion MRS and MRI of fibers in bovine optic nerve and in rat brain *in vivo*. *Proc. Int. Soc. Magn. Reson. Med.* 1998; **6**: 1263.

63. Assaf Y, Cohen Y. *In vivo* and *in vitro* bi-exponential diffusion of N-Acetyl Aspartate (NAA) in rat brain: a potential structural probe? *NMR Biomed.* 1998; **11**: 67–74.

64. Assaf Y, Cohen Y. Structural information of neuronal tissue as revealed by *q*-space diffusion NMR spectroscopy of metabolites in bovine optic nerve. *NMR Biomed.* 1999; **12**: 335–344.

65. Assaf Y, Cohen Y. The sources of diffusion components in neuronal tissue: application to white matter disorders. *Proc. Int. Soc. Magn. Reson. Med.* 1999; **7**: 555.

66. Assaf Y, Cohen Y. Assignment of the water slow diffusing component in CNS using q-space diffusion MRS: Implications to fiber tract imaging. *Magn. Reson. Med.* 2000; **43**: 191–199.

67. Assaf Y, Michal K, Shinar H, Chapman J, Korczyn AD, Navon G, Cohen Y. Changes in axonal morphology in experimental allergic neuritis as studied by q-space ^{1}H and ^{2}H DQF diffusion magnetic resonance spectroscopy. *Magn. Reson. Med.* 2002; **48**: 71–81.

68. Assaf Y, Mayk A, Cohen Y. Displacement imaging of spinal cord using q-space diffusion weighted MRI. *Magn. Reson. Med.* 2000; **44**: 713–722.

69. Assaf Y, Mayk A, Cohen Y. MRI of demyelination in stroke prone spontaneous hypertensive rats. *Proc. Int. Soc. Magn. Reson. Med.* 2000; **8**: 401.

70. Amar K, Wilcock G. Vascular dementia. *Br. Med. J.* 1996; **312**: 227–231.

71. van Gijn J. Leukoariosis and vascular dementia. *Neurology* 1998; **51**: 53–58.

72. Nossin-Manor R, Duvdevani R, Oz R, Cohen Y. Displacement imaging of hemi-crush in rat spinal cord using heavily diffusion-weighted MRI. *Proc. Int. Soc. Magn. Reson. Med.* 2001; **9**: 150.

73. Nossin-Manor R, Duvdevani R, Cohen Y. q-Space high *b*-value diffusion MRI of hemi-crush in rat spinal cord: Evidence for spontaneous regeneration. *Magn. Reson. Imag.* 2002; **20**: 231–241.

74. Horner PJ, Gage FH. Regenerating the damaged central nervous system. *Nature* 2000; **407**: 963–970.

75. Ditunno JF, Graziani V, Tessler A. Neurological assessment of spinal cord injury. *Adv. Neurol.* 1997; **72**: 325–333.

76. Fenyes DA, Narayana PA. In vivo diffusion characteristics of rat spinal cord. *Magn. Reson. Imag.* 1999; **17**: 717–722.

77. Franconi F, Lemaire L, Marescaux L, Jallet P, Le Jeune JJ. In vivo quantitative micro-imaging of rat spinal cord at 7T. *Magn. Reson. Med.* 2000; **44**: 893–898.

78. Inglis BA, Yang L, Wirth III Ed, Plant D, Mareci TH. Diffusion anisotropy in excised normal rat spinal cord measured by NMR microscopy. *Magn. Reson. Imag.* 1997; **15**: 441–450.

79. Ries M, Jones RA, Dousset V, Moonen CTW. Diffusion tensor MRI of the spinal cord. *Magn. Reson. Med.* 2000; **44**: 884–892.

80. Phillips JT. Rethinking multiple sclerosis. *Arch. Neurol.* 2001; **58**: 30–32.

81. Bastin ME, Armitage PA, Marshall I. A theoretical study of the effect of experimental noise on the measurements of anisotropy in diffusion imaging. *Magn. Reson. Imag.* 1998; **16**: 773–785.

82. Maier SE, Vajapeyam S, Mamata H, Westin C, Jolesz FA, Mulkern R. Diffusion tensor imaging of the fast and slow diffusion coefficient components in human brain. *Proc. Int. Soc. Magn. Reson. Med.* 2001; **9**: 503.

83. Clark CA, Hedeus M, Moseley M. In vivo mapping of the fast and slow diffusion tensors in human brain. *Proc. Int. Soc. Magn. Reson. Med.* 2001; **9**: 167.

84. Fazekas F, Barkhof F, Filippi M, Grossman RI, Li DKB, McDonald WI, McFarland HF, Paty DW, Simon JH, Wolinsky JS, Miller DH. The contribution of magnetic resonance imaging to the diagnosis of multiple sclerosis. *Neurology* 1999; **53**: 448–456.

85. Barkhof F, van Walderveen M. Characterization of tissue damage in multiple sclerosis by nuclear magnetic resonance. *Phil. Trans. R. Soc. Lond. B* 1999; **354**: 1675–1686.

86. Cucurella MG, Rovira A, Rio J, Pedraza S, Tintore MM,

Montalban X, Alonso J. Proton magnetic resonance spectroscopy in primary and secondary progressive multiple sclerosis. *NMR Biomed.* 2000; **13**: 57–63.

87. Leary SM, Davie CA, Parker GJM, Stevenson VL, Wang LQ, Barker GJ, Miller DH, Thompson AJ. H-1 Magnetic resonance spectroscopy of normal appearing white matter in primary progressive multiple sclerosis. *J. Neurol.* 1999; **246**: 1023–1026.

88. Tortorella C, Viti B, Bozzali M, Sormani MP, Rizzo G, Gilardi MF, Comi G, Filippi M. A magnetization transfer histogram study of normal-appearing brain tissue in MS. *Neurology* 2000; **54**: 186–193.

89. Assaf Y, Ben-Bashat D, Chapman J, Peled S, Biton IE, Kafri M, Segev Y, Hendler T, Korczyn AD, Graif M, Cohen Y. High *b*-value q-space analyzed diffusion-weighted MRI: Application to multiple sclerosis. *Magn. Reson. Med.* 2002; **47**: 115–126.

90. Li TQ, Haggkvist M, Odberg L. Porous structure of cellulose fibers studied by q-space NMR imaging. *Langmuir* 1997; **13**: 3570–3574.

91. Callaghan PT, Eccles CD, Xia Y. NMR microscopy of dynamic displacements: k-space and q-space imaging. *J. Phys. E* 1988; **21**: 820–822.

92. Jenner CF, Xia Y, Eccles CD, Callaghan PT. Circulation of water within wheat-grain revealed by nuclear magnetic resonance micro-imaging. *Nature* 1988; **336**: 399–402.

93. Scheenen TWJ, van Dusschoten D, de Jager PA, Van As H. Microscopic displacement imaging with pulsed field gradient turbo spin-echo NMR. *J. Magn. Reson.* 2000; **142**: 207–215.

94. Scheenen TWJ, Vergeldt FJ, Windt CW, de Jager PA, Van As H, Microscopic imaging of slow flow and diffusion: A pulsed field gradient stimulated echo sequence combined with turbo spin echo imaging. *J. Magn. Reson.* 2001; **151**: 94–100.

95. Tuch DS, Wiegell MR, Reese TG, Beliveau JW, Wedeen VJ. Measuring cortico-cortical connectivity matrices with diffusion spectrum imaging. *Proc. Int. Soc. Mag. Reson. Med.* 2001; **9**: 502.

96. Wiegell MR, Reese TG, Tuch DS, Sorensen AG, Wedeen VJ. Diffusion spectrum imaging of fiber white matter degeneration. *Proc. Int. Soc. Mag. Reson. Med.* 2001; **9**: 504.